CENTRO DE INVESTIGACIONES EN OPTICA, A.C.

"ENTANGLED TWO PHOTON STATE IN A HELICAL INCE-GAUSS BASIS"

Versión Definitiva. Incluye cambios sugeridos por revisores.

Tesis que para obtener el grado de Maestro en Ciencias (Óptica)

Presenta: Aarón Adrián Aguilar Cardoso

Director de Tesis: Dr. Roberto Ramírez A.

León · Guanajuato · México
Julio de 2023

"The most exciting phrase to hear in science, the one that heralds new discoveries, is not 'Eureka!' but 'That's funny...' "

Isaac Asimov

Abstract

Spontaneous Parametric Down Conversion (SPDC) is a process that generates photons pairs that are entangled in several degrees of freedom, in particular, the entanglement given by the conservation of Orbital Angular Momentum (OAM) is one of the most explored nowadays, given its infinite-dimensional basis of the Hilbert space. Since the natural basis of the OAM are the Laguerre-Gauss modes, the OAM entangled state of this process is described in these modes. Since it has been suggested that these modes have the capability to tune the probability detection of the entangled photons, in this thesis we perform a change of basis of the photon-pair entangled state, generated by SPDC, and describe it in terms of Helical Ince-Gauss modes. With this change of basis, we are able to describe how the probability detection of the photon pair can be tuned with the ellipticity parameter of these modes. We also found that, on this basis, the state has two different Bell states, and it is possible to switch from one Bell state to another. In order to verify that it is possible to tune the probability detection, and also, that we can switch from one Bell state to another, we build a source of entangled photon pairs, and measure the tuning of the probability detection and confirm the entanglement of the state with a Bell-type inequality test.

Acknowledgements

Special thanks to my brother, my mother, and my dog, who even being far away, were always present.

Contents

List of Figures

vi

List of Tables

Abbreviations

APD   Avalanche Photo Detector

BBO   Beta Barium Borate

BS   Beam Splitter

EPR   Einstein Podolsky Rosen

HG   Hermite-Gauss

HIG   Helical Ince-Gauss

IG   Ince-Gauss

KEM   Knife Edge Mirror

LG   Laguerre-Gauss

OAM   Orbital Angular Momentum

PWE   Paraxial Wave Equation

SLM   Spatial Light Modulator

SMF   Single Mode Fiber

SPDC   Spontaneous Parametric Down Conversion

Introduction

Quantum mechanics has proven to be one of the most important branch of physics, since this theory have provided us with a better understanding of nature itself. Moreover, predictions given by quantum mechanics have astonished the scientific community even in the early days of its invention, since it challenges our classical intuition about how objects interact, which arises from the probabilistic nature of this theory.

Entanglement is a fundamental concept in quantum mechanics, and is the essence of this thesis [1–3]; in this phenomenon two or more particles become correlated in such a way that the state of one particle cannot be described independently of the state of the other. If the particles are entangled, their properties become intertwined, regardless of the physical distance between them. This notion of "spooky action at a distance" captured the physics community's attention, initiating a heated debate about the veracity of this theory. In 1935, Albert Einstein, along with Boris Podolsky, and Nathan Rosen, wrote a groundbreaking paper, nowadays known as the EPR, where they introduced a thought experiment involving a pair of entangled particles, which exhibited correlations that seemed to defy classical notions of locality and realism [4]. They argued that such phenomenon between the particles is due to unknown variables of the system, nowadays known as hidden variables, which determine the outcomes of measurements on entangled particles.

Nearly 50 years later, the experimental existence of entanglement became possible [5, 6]. In 1964, John Bell demonstrated mathematically that no theory based on local hidden variables could reproduce all the predictions of quantum mechanics, by showing that if certain statistical correlations, known as Bell inequalities, are violated in experimental measurements, it is not possible to explain those correlations using local hidden variables, which would validate the quantum mechanics theory and, subsequently, entanglement .

The most famous and widely used version of Bell's inequality is the CHSH inequality, proposed by John Clauser, Michael Horne, Abner Shimony, and Richard Holt in 1969 [7].

This inequality sets a limit on the correlations that can be obtained in experiments involving entangled particles with binary measurements, and to prove this inequality they proposed an experiment with a pair of photons entangled in their polarization degree. Such experiment was done until 1981 by Aspect *et al.* [8], confirming the polarization's photon entanglement and violating for the first time in history a Bell inequality.

In recent years, the study of entanglement has expanded beyond traditional degrees of freedom like spin and polarization, leading researchers to explore alternative entanglement degrees of freedom than polarization, such as energy-time entanglement [9, 10], momentum-position entanglement [11], and frequency-transverse momentum entanglement [12]. The particles can also be entangled in Orbital Angular Momentum (OAM) degree of freedom [13, 14], such photon-pair entangled state can be obtained with Spontaneous Parametric Down-Conversion (SPDC) process [15]. The SPDC is a quantum phenomenon in which a photon is converted into two lower-energy photons. In this process the total OAM of the three photons is conserved, converting the OAM of the initial photon into the OAM of the entangled photon pair, allowing for the generation of entangled photon pairs with well-defined OAM states. This was confirmed in 2001 by Mair *et al.* [16], where it was established that the two photon state is not a mixture, but a coherent superposition of product Laguerre-Gauss (LG) modal states that obeys OAM conservation, this is because LG modes has well defined OAM [17–19]. As the combination of OAM values of the SPDC photon pair is infinite, the two photon state, described as superposition of Laguerre-Gauss modes, represents a high-dimensional entangled state, as it defines a discrete Hilbert space with infinite dimension [20]. This high-dimensional entangled state have potential applications in materials engineering [21, 22] and quantum information [23, 24].

By exploring alternative bases, other than LG, such as Hermite-Gauss (HG) modes [25], Bessel-Gauss (BG) modes [26], and Hermite-Laguerre-Gaussian (HLG) modes [27], we seek to uncover new insights into the nature of entanglement of SPDC photon-pairs. A base in which the two photon state, given by SPDC, has not been studied yet, is the Helical Ince-Gauss (HIG) modes [28, 29]. The Ince-Gauss (IG) modes are a exact, complete, and orthogonal solution to the paraxial wave equation solved in elliptical coordinates. A superposition of the IG modes gives us the Helical Ince-Gauss modes, which, by the superposition principle, are also solution to the paraxial wave equation. The main characteristic of HIG modes, is that these modes represents the transition between the Laguerre-Gauss modes and the Hermite-Gauss modes, since the elliptical coordinates also include the Cartesian coordinates as well as cylindrical coordinates, which are the coordinate systems

in which the HG and LG are described, respectively. The HIG modes have unique properties, for instance, it has been proved that HIG modes can tune the OAM value of a single photon [30], which makes them interesting candidates to study OAM entanglement.

In this thesis we provide a theoretical description of the photon-pair entangled state, given by SPDC, in terms of Helical Ince-Gauss modes. Our main motivation to do this is that as HIG modes can tune the OAM, then HIG modal probability, of this entangled state, should be tunable as well. This probability tuning was suggested experimentally by Krenn *et al.* [31], with no proper explanation, since they considered this quantum state as a particular Bell state described in HIG modes, removing all the richness offered by the true description of the state in these modes.

In order to develop a theoretical description of the SPDC photon pair state, we perform a change of basis of the photon-pair entangled state, and describe it in terms of Helical Ince-Gauss modes. We will find that this quantum state can be described as a sum of two HIG Bell states, whose coefficients are dependent on the ellipticity used for the HIG basis, which confirms that it is also possible to tune the modal probability of the state. Even more, it is demonstrated, that in this description, it is possible to pass from one HIG Bell state to another, by adjusting the ellipticity of the used basis, so it is possible to approximate this state as a specific HIG Bell state, only under certain ellipticity values.

In order to confirm this description we develop a SPDC experiment, and by projecting the two photon state in to HIG modes, we measure the HIG modal probability of the photon-pair entangled state. By changing the ellipticity of the HIG modes we compare the results with the theoretical description, thus confirming, not only theoretically, but also experimentally, that it is possible to tune the modal probability of the state.

Finally by performing a Bell test, and violating a Bell-type inequality, we confirm this modal entanglement and so the description of this quantum state.

Chapter 1

Theoretical Background

In order to describe the behavior of the photon-pair entangled state, generated by SPDC, in the Helical Ince-Gaussian basis, it is important to clarify every aspect of what this means. So first we discuss what a spatial mode is, by reviewing the origin and meaning of the paraxial wave equation. Understanding the paraxial wave equation is crucial for grasping the principles behind SPDC and the subsequent generation of entangled states. Then we show the distinct solutions to it, known as spatial modes. With special emphasis on Laguerre-Gauss modes and Helical Ince-Gauss modes.

Given that the focus of our investigation revolves around the degree of freedom of Orbital Angular Momentum in the SPDC process, a dedicated section will be allocated to its in depth exploration. Special attention will be given to the OAM that certain spatial modes carry, as it plays a vital role in understanding the main aspect of this work.

The entanglement of the two photon state is characterized by the correlations between two photons. Since this state is generated by the SPDC process, we will explain the nature of the state through this experimental process, as well as its description in terms of the Laguerre-Gauss modes.

The properties of one of the down converted photons become instantaneously correlated with the properties of the other photon, regardless of the physical distance between them. In order to fully understand this phenomenon, here we discuss deeply what entanglement is and how can it be confirmed in an experiment.

1.1 Paraxial Wave Equation (PWE)

The electric and magnetic components of light are described by complex fields $\vec{E}$ and $\vec{B}$ respectively, and, according to Maxwell equations, these fields satisfy the wave equation [32]

$$\nabla^2 \vec{E} - \frac{1}{c^2}\frac{\partial^2}{\partial t^2}\vec{E} = 0, \tag{1.1}$$

$$\nabla^2 \vec{B} - \frac{1}{c^2}\frac{\partial^2}{\partial t^2}\vec{B} = 0. \tag{1.2}$$

here c is the speed of light in vacuum. By making the assumption that the temporal dependence of the fields is $\vec{E} = E_i(\vec{r})e^{i\omega t}\hat{e}_i$, and by substituting this in Eq. 1.1, then we find the scalar Helmholtz equation

$$\nabla^2 E_i(\vec{r}) + k^2 E_i(\vec{r}) = 0, \tag{1.3}$$

here $k = n\omega/c$ is the wave number, n is the refractive index, and ω is the angular frequency of the light wave. Assuming that the dependence of the wave amplitude change slowly in the direction of propagation in contrast with the change in the perpendicular directions, hence $k_z \gg k_x, k_y$, therefore

$$k_z \approx k - \frac{k_x^2 + k_y^2}{2k}. \tag{1.4}$$

These considerations are known as the paraxial approximation. We consider a function, solution to Eq. 1.3, as

$$E_i(\vec{r}) = u(\vec{r})e^{ikz}, \tag{1.5}$$

where $u(\vec{r})$ represents the complex-valued amplitude which modulates the sinusoidal plane wave represented by the exponential factor, and contains the distribution of the field in space, and with the paraxial approximation the z derivative of this amplitude function is a slowly varying function of z, then we can neglect the second derivative respect to z. So substituting Eq. 1.5 into Eq. 1.3 we get

$$\nabla_t^2 u(\vec{r}) + 2ik\frac{\partial}{\partial z}u(\vec{r}) = 0, \tag{1.6}$$

here $\nabla_t^2 = \frac{\partial^2}{\partial x^2} + \frac{\partial^2}{\partial y^2}$. Equation 1.6 is called the Paraxial Wave Equation (PWE) and, as we will discuss in section 1.2.2, which solutions are the main component of the present work. In the next subsections we discuss three main solutions of the PWE, relevant to the present work.

1.1.1 Hermite-Gauss Modes (HG)

In order to solve Eq. 1.6 in cartesian coordinates (x, y, z) a general solution might be written in the form of separate functions, each one depending on one transverse variable x and y. A normalized solution is given by the Hermite-Gauss modes [13]

$$HG_{n_x,n_y}(x,y,z) =$$

$$\sqrt{\frac{1}{2^{n_x+n_y-1}\pi n_x! n_y!}} \frac{1}{\omega(z)} H_{n_x}\left(\frac{\sqrt{2}x}{\omega(z)}\right) H_{n_y}\left(\frac{\sqrt{2}y}{\omega(z)}\right) e^{\frac{-r^2}{\omega^2(z)}} e^{i(kz+\frac{kr^2}{2R(z)}-(n_x+n_y+1)\psi_g(z))},$$

$$(1.7)$$

where $w(z)$ is the beam waist, $R(z)$ is the radius of curvature of the phase front, $\psi_g(z)$ is the Gouy phase and H_n is the Hermite polynomial of order n.

The transverse structure of Hermite-Gauss modes can be described by two integers, denoted as n_x and n_y, which determine the number of nodes in the x and y directions, respectively. These integers are related to the order of the Hermite polynomials that describe the x and y variations of the electric field, so Hermite polynomials represent the spatial variation of the electric field in the transverse plane, and they are orthogonal to each other. Examples of intensity distributions of Hermite-Gauss modes are depicted in Fig. 1.1.

(a) $|HG_{0,5}(\vec{r})|^2$ (b) $|HG_{2,3}(\vec{r})|^2$ (c) $|HG_{4,1}(\vec{r})|^2$
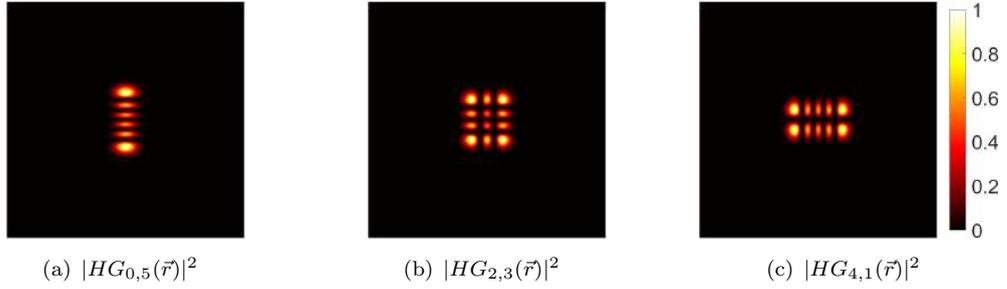
FIGURE 1.1: Transverse intensity distributions of HG modes for $n_x = 0, n_y = 5$, $n_x = 2, n_y = 3$ and $n_x = 4, n_y = 1$.

HG modes are orthonormal to each other, meaning that the integral of the product of two different HG modes over the transverse plane is zero [13]

$$\int\int_{-\infty}^{\infty} HG_{n_x,n_y}(x,y,z) HG^*_{n'_x,n'_y}(x,y,z) dx dy = \delta_{n_x n'_x} \delta_{n_y n'_y}, \quad (1.8)$$

this orthonormality property is advantageous for analyzing and decomposing complex laser beams into their constituent HG mode components. It facilitates the efficient representation of laser beams and enables the use of HG modes as a basis for expansion and analysis. These properties make them useful for various applications, such as laser engineering [33], optical communications [34], metrology [35], and quantum optics [25, 36].

1.1.2 Laguerre-Gauss Modes (LG)

If we solve the Paraxial Wave Equation in cylindrical coordinates (r, ϕ, z), the normalized solution are the Laguerre-Gauss modes [13]

$$LG_{l,n}(\vec{r}) =$$

$$\sqrt{\frac{2n!}{\pi(n+|l|)!}} \frac{1}{\omega(z)} \left(\frac{r\sqrt{2}}{\omega(z)}\right)^{|l|} e^{\frac{-r^2}{\omega^2(z)}} L_n^{|l|}\left(\frac{2r^2}{\omega^2(z)}\right) e^{i\left(kz + \frac{kr^2}{2R(z)} - (2n+|l|+1)\psi_g(z)\right)} e^{il\phi}. \qquad (1.9)$$

As it is shown, the Laguerre-Gauss modes are also solutions to the paraxial wave equation, just like Hermite-Gauss modes. However, they have a different transverse mode structure, which can be described by a set of Laguerre polynomials. The transverse structure of Laguerre-Gauss modes can be described by two integers, denoted as n and l, which determine the number of nodes in the radial and azimuthal directions, respectively. These integers are related to the order of the Laguerre polynomials that describe the radial and azimuthal variations of the electric field.

Laguerre-Gauss have a well-defined beam waist and a propagation invariant profile, which makes them useful for applications that require a stable and focused beam, such as optical communications [37, 38], metrology [39], and quantum optics [16–19, 40]. As will be explained in the next section, individual photons on Laguerre-Gauss modes carry integer values of Orbital Angular Momentum, given by the azimuthal number as $l\hbar$; this arises from the azimuthal phase variation of the electric field. This property makes them useful for applications such as optical communication, where the OAM can be used to encode information in the spatial domain [41].

Examples of intensity distributions of Laguerre-Gauss modes are depicted in Fig. 1.2. The radial number n dictates the number of "donuts" that the mode has, as $n + 1$. While the azimuthal number l dictates the number of steps that the helical phase has.

LG modes are orthonormal to each other [13]

(a) $|LG_{5,0}(\vec{r})|^2$ (b) $|LG_{3,1}(\vec{r})|^2$ (c) $|LG_{1,2}(\vec{r})|^2$

(d) $LG_{5,0}(\vec{r})$ phase   (e) $LG_{3,1}(\vec{r})$ phase   (f) $LG_{1,2}(\vec{r})$ phase

FIGURE 1.2: Transverse intensity distributions of LG modes with its respective phase for $l = 5, n = 0$, $l = 3, n = 1$ and $l = 1, n = 2$.

$$\int_0^{2\pi} \int_0^{\infty} LG_{l,n}(\vec{r}) LG^*_{l',n'}(\vec{r}) r \, dr \, d\phi = \delta_{ll'} \delta_{nn'}, \tag{1.10}$$

this orthonormality property, will be fundamental in the following sections to explain modal entanglement.

Another possible solution to Eq. 1.6 on cylindrical coordinates is given by even and odd Laguerre-Gauss modes

$$LG_{l,n}^{e,o}(\vec{r}) =$$

$$\sqrt{\frac{4n!}{(1 + \delta_{0,l})\pi(n+l)!}} \frac{1}{\omega(z)} \left(\frac{r\sqrt{2}}{\omega(z)} \right)^l e^{\frac{-r^2}{\omega^2(z)}} L_n^l \left(\frac{2r^2}{\omega^2(z)} \right) e^{i(kz + \frac{kr^2}{2R(z)} - (2n+l+1)\psi_g(z))} \begin{bmatrix} \cos(l\phi) \\ \sin(l\phi) \end{bmatrix}. \tag{1.11}$$

These even and odd Laguerre-Gauss modes will be used in section 2.2, in order to make the change of basis. It should be noted that these modes do not carry defined OAM, only the regular ones does.

1.1.3 Ince-Gauss Modes (IG)

Another solution to Eq. 1.6 arises from solving it in elliptical coordinates (ξ, η, z), a normalized solution are the even and odd Ince-Gauss modes [28, 29]

$$IG_{p,m}^e(\vec{r}, \epsilon) = \frac{C\omega_0}{\omega(z)} C_p^m(i\xi, \epsilon) C_p^m(\eta, \epsilon) e^{\frac{-r^2}{\omega^2(z)}} e^{i(kz + \frac{kr^2}{2R(z)} - (p+1)\psi_g(z))}, \tag{1.12}$$

$$IG_{p,m}^o(\vec{r}, \epsilon) = \frac{S\omega_0}{\omega(z)} S_p^m(i\xi, \epsilon) S_p^m(\eta, \epsilon) e^{\frac{-r^2}{\omega^2(z)}} e^{i(kz + \frac{kr^2}{2R(z)} - (p+1)\psi_g(z))}, \tag{1.13}$$

here C_p^m and S_p^m are solutions of the Ince differential equation, so they are known as the even and odd Ince polynomials respectively, where $0 < m < p$ for even functions, $1 < m < p$ for odd functions, the indices (p, m) always have the same parity, and ϵ is the ellipticity parameter.

Ince-Gauss modes are exact and orthogonal solutions to the PWE, less well-known than Hermite-Gauss and Laguerre-Gauss modes. The transverse mode structure of Ince-Gauss modes can be described by three parameters, denoted as p, m, and ϵ, which together determine the asymmetry and ellipticity of the mode, respectively. The transverse profile of an Ince-Gauss mode can take on a variety of shapes as seen in Fig. 1.3.

(a) $|IG_{3,3}^e(\vec{r}, 3)|^2$ (b) $|IG_{6,2}^e(\vec{r}, 3)|^2$ (c) $|IG_{9,5}^e(\vec{r}, 3)|^2$

(d) $|IG_{3,3}^o(\vec{r}, 3)|^2$ (e) $|IG_{6,2}^o(\vec{r}, 3)|^2$ (f) $|IG_{9,5}^o(\vec{r}, 3)|^2$
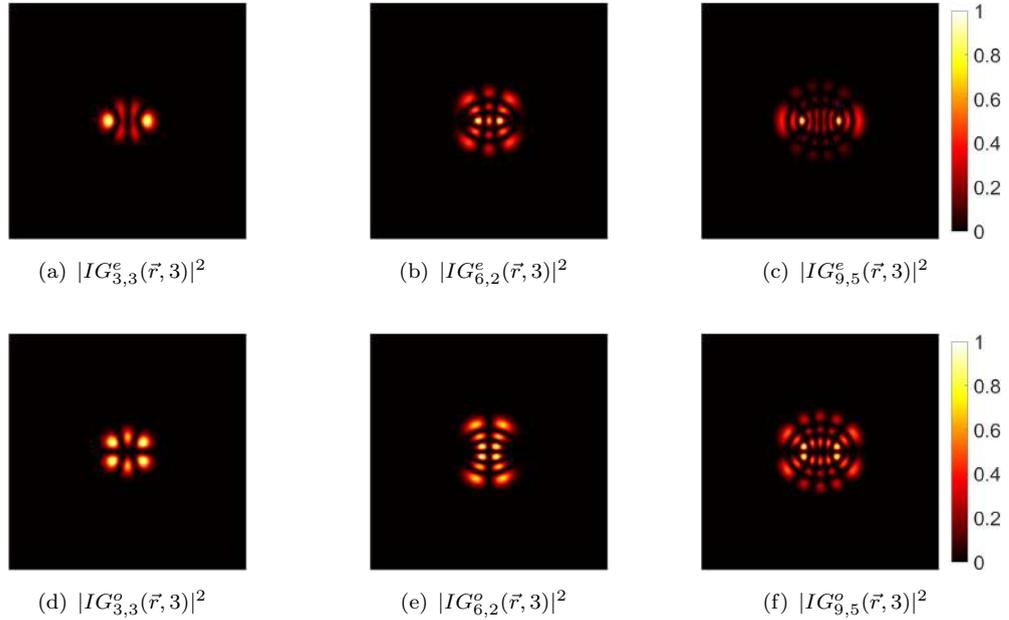
FIGURE 1.3: Transverse intensity distributions of even and odd IG modes with $\epsilon = 3$, for $p = 5, m = 3$, $p = 6, m = 2$ and $p = 9, m = 5$.

These modes have unique properties, given control of the ellipticity of the mode. By adjusting ϵ, one can tune the shape of the mode from circular to rectangular. This control enables the generation of laser beams with specific elliptical profiles tailored to the requirements of various applications, such as optical communications [42], optical trapping [43], materials engineering [44], and quantum optics [31, 45, 46].

IG modes are orthonormal to each other [28, 29]

$$\int \int_{-\infty}^{\infty} IG_{p,m}^{\sigma}(\vec{r}, \epsilon) IG_{p',m'}^{\sigma',*}(\vec{r}, \epsilon') \mathbf{dS} = \delta_{\sigma\sigma'}\delta_{pp'}\delta_{mm'}, \tag{1.14}$$

here σ is the parity of the mode (e,o). Note that ellipticity does not appear in the orthonormality condition. As we will discuss later, we are going to take advantage of this orthonormality property to be able to tune the probability detection of the two photon state, given by SPDC.

The ellipticity is quite a unique parameter, since it can take continuous values, contrary to p and m. Even more, since the elliptic coordinates can approximate to cylindrical and cartesian coordinates, the relation of Ince-Gauss modes with the Hermite and Laguerre Gaussian modes is given via the ellipticity; larger absolute values result in a more pronounced elliptical profile, while smaller values indicate a closer approximation to a circular shape. So in the limit $\epsilon \to 0$ the elliptic coordinates tend to the circular cylindrical coordinates, and so the even and odd Ince-Gauss modes tend to the even and odd Laguerre-Gauss modes with the indices relations: $m = l$ and $p = 2n + l$. On the contrary limit, $\epsilon \to \infty$, the elliptic coordinates tend to the cartesian coordinates, in this case, the even and odd Ince-Gauss modes tend to Hermite-Gauss modes with the indices relations: $n_x = m$ and $n_y = p - m$ for even Ince-Gauss, and $n_x = m - 1$ and $n_y = p - m + 1$ for odd Ince-Gauss. This transition is depicted in Fig. 1.4.

(a) $|IG_{5,3}^e(\vec{r}, \epsilon \to 0)|^2 \to |LG_{3,1}^e|^2$ (b) $|IG_{5,3}^e(\vec{r}, 2)|^2$ (c) $|IG_{5,3}^e(\vec{r}, \epsilon \to \infty)|^2 \to |HG_{3,2}|^2$
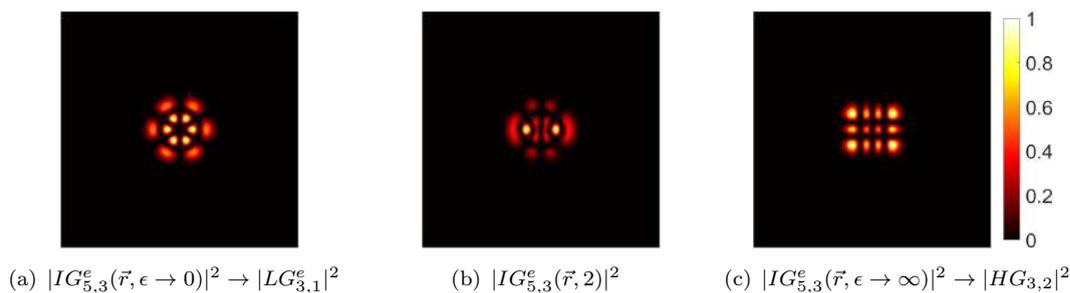
FIGURE 1.4: Transition from $LG_{3,1}^e$ to $IG_{5,3}^e$ to $HG_{3,2}$.

As these modes are complete families solutions to Eq. 1.6 we are able to express any Ince-Gauss mode as a specific superposition of either Laguerre-Gauss modes and Hermite Gauss modes. However, we are only interested in the former case, which is given by

$$IG_{p,m}^{\sigma}(\vec{r}, \epsilon) = \sum_{n,l} D_{ln}^{\sigma}(\epsilon) LG_{l,n}^{\sigma}, \qquad (1.15)$$

where σ represents the parity (even or odd) of the mode, D_{ln} are the weights of the Laguerre-Gauss expansion; these required terms are given by the constraint that $p = 2n+l$, and can be written as [28, 29]

$$D_{ln}^{\sigma}(\epsilon) = \mathfrak{D}(-1)^{l+n+(p+m)/2} \sqrt{(1+\delta_{0l})(n+l)!} A_{(l+\delta_{\sigma 0})/2}^{\sigma}(\epsilon), \qquad (1.16)$$

where $A_{(l+\delta_{\sigma 0})/2}^{\sigma}(\epsilon)$ is the $(l+\delta_{\sigma 0})/2$ th Fourier coefficient of the Ince polynomial associated with the beam, this coefficient depends explicitly on the ellipticity. The normalization constant $\mathfrak{D}$ is found with the condition $\sum_{l,n} D_{ln}^{\sigma 2}(\epsilon) = 1$. This coeffcents are calculated numerically with a MATLAB code (see Apppendix A). With this expansion we are capable to perform a change of basis of a system based on Laguerre-Gauss modes.

1.1.4   Helical Ince-Gauss Modes (HIG)

An important property of Laguerre-Gauss modes, as it will be pointed out in the next section, is that they carry integer values of Orbital Angular Momentum $l\hbar$, because of its azimuthal angular dependence $e^{il\phi}$, meanwhile, Hermite-Gauss and Ince-Gauss beams do not have such dependence. In order to build Ince-Gaussian modes with a rotating phase, like Laguerre-Gauss modes (Fig. 1.2 d, e, f), Bandres *et al.* [28] defined the Helical Ince-Gauss modes as

$$HIG_{p,m}^{\pm}(\vec{r}, \epsilon) = \frac{1}{\sqrt{2}} \left(IG_{p,m}^{e}(\vec{r}, \epsilon) \pm iIG_{p,m}^{o}(\vec{r}, \epsilon) \right). \qquad (1.17)$$

The sign $\pm$ of this spatial function defines the phase rotating direction, where $+$ sign rotate the phase counterclockwise, and the $-$ sign rotate the phase clockwise.

For this family of solutions, the values of $m = 0$ is not allowed, since the odd mode $IG_{p,m}^{o}$ is not defined for this value. The transverse profile of Helical Ince-Gauss modes are shown in Fig. 1.5, with the respective phase distribution. The number of elliptical rings is given by $1 + (p - m)/2$, and each ring splits in single nodes as the ellipticity increase.

(a) $|HIG^+_{4,2}(\vec{r},3)|^2$ (b) $|HIG^-_{5,3}(\vec{r},3)|^2$ (c) $|HIG^+_{7,5}(\vec{r},3)|^2$

(d) $HIG^+_{4,2}(\vec{r},3)$ phase   (e) $HIG^-_{5,3}(\vec{r},3)$ phase   (f) $HIG^+_{7,5}(\vec{r},3)$ phase
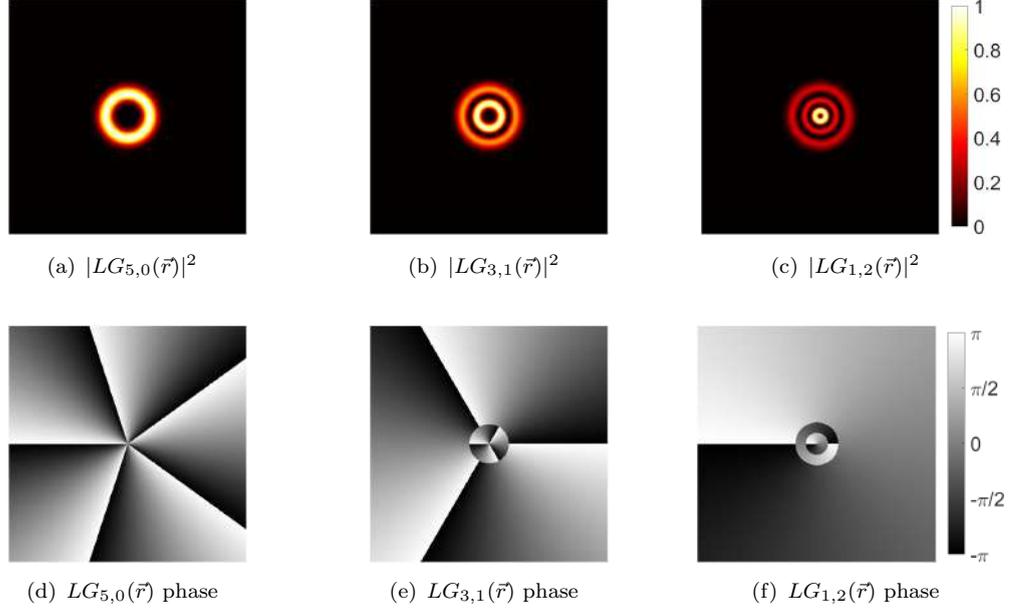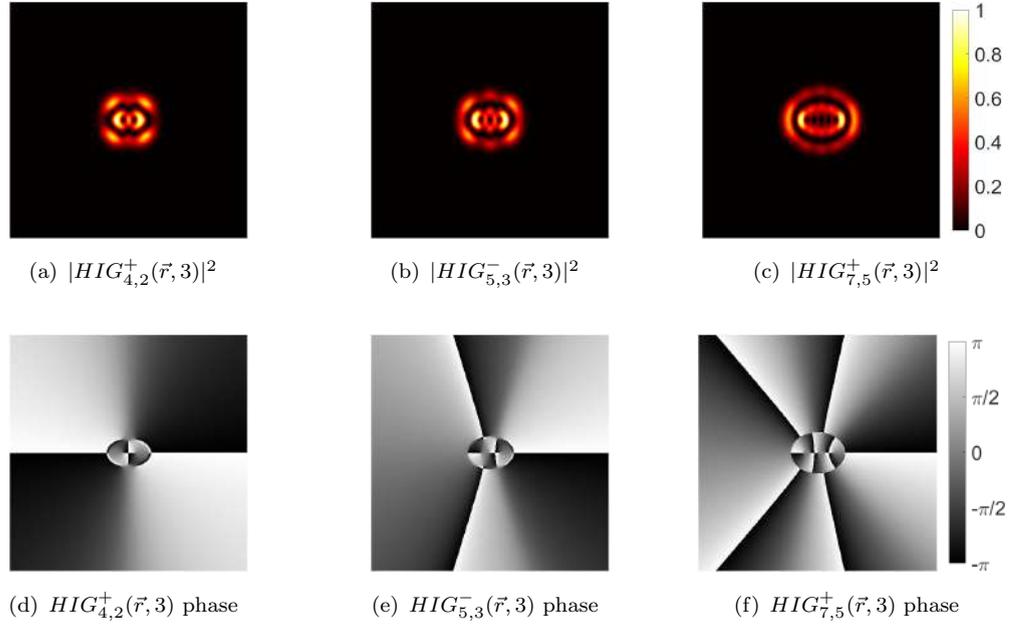
FIGURE 1.5: Transverse intensity distributions of LG modes with its respective phase for $l = 3, n = 5$, $l = 3, n = 1$ and $l = 1, n = 2$.

1.2 Orbital Angular Momentum (OAM)

After Maxwell developed the theory of electromagnetism, many scientists took advantage of it and began exploring the electromagnetic field's physical properties. One of the main topics in which the physisicist where interested in, were the mechanical effects of light, in fact, the idea that light has mechanical properties was already discussed in the early years of the study of radiation, with no proper explanation. It was John Henry Poynting who found the relation between the energy stored in the electromagnetic field and the work done on a charge distribution, this through energy flux [47].

Once it was established that electromagnetic fields have momentum, it is natural to ask if it also has angular momentum. In fact, the light has two contributions to its angular momentum; one that is related to the polarization of the field, known as Spin Angular Momentum (SAM), and the part that is determined solely by the azimuthal phase dependence, which is known as Orbital Angular Momentum (OAM). The angular momentum has vast applications which are promising in branches such as micro-manipulation [48], nonlinear interactions [49], imaging [50], sensing [51], quantum [23] and classical communications [52].

The aim of this section is to discuss the theory of Orbital Angular Momentum and its relation to the Helical Ince-Gauss modes.

1.2.1 Classic OAM

A direct consequence that electromagnetic field carries energy itself is that the field also carries momentum. It is well known from Maxwell and Poynting's theories that the momentum density in the fields, on free space, is given by [13]

$$\vec{P} = \epsilon_0 \vec{E} \times \vec{B}. \tag{1.18}$$

By taking a particular case, but still a very realistic one, is possible to calculate the angular contribution of electromagnetic field, in order to show the physical nature of orbital angular momentum of light. Taking the case in which the field is monochromatic light, travels in one direction (z axis), is linearly polarized, and with the paraxial approximation, the time-averaged momentum density is

$$\langle \vec{p} \rangle = \frac{\epsilon_0 \omega k}{2} \left[2|u|^2 \hat{z} + \frac{i}{k}(u\nabla u^* - u^*\nabla u) \right]. \tag{1.19}$$

The time-averaged momentum points in a direction not always perpendicular to the z axis, in fact, a detailed examination of this expression show that at a constant radius, the pointing vector has an spiral path of well-defined pitch (Fig. 1.6).
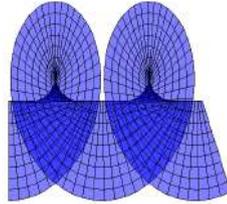
FIGURE 1.6: The spiraling curve represents the Poynting vector of a linearly polarized Laguerre-Gauss mode.

The time-averaged total angular momentum density can be obtained by considering a field with an explicit azimuthal dependence such as $u = u_0 e^{il\phi}$ where l is an integer. Concentrating on the z-component of the cross product of ϕ-component of the time-averaged momentum density with $\vec{r}$, the time-averaged total angular momentum density is

$$\langle j_z \rangle = \epsilon_0 \omega l |u|^2. \tag{1.20}$$

With $c = \frac{\omega}{k}$, we can obtain the ratio of the angular momentum and the energy per unit length of the beam

$$\frac{\langle J_z \rangle}{c \langle P_z \rangle} = \frac{l}{\omega}. \tag{1.21}$$

In the next subsection it will be clarified that, from this expression, l describes the OAM per photon, so Eq. 1.21 is the ratio of the total Orbital Angular Momentum and the energy per photon. Nevertheless, in a macroscopic point of view Eq. 1.21 can be considered as the ratio of the orbital angular momentum flux to the energy flux, which is a natural description of the angular momentum carried by light beams.

As it was shown through this derivation, the Orbital Angular Momentum is a direct consequence that a mode of light has an azimuthal dependence of $e^{il\phi}$ (with l as an integer). These are called helically phased beams and implies two remarkable characteristics; that the beam axis is a phase singularity from where the optical phase changes by $2\pi l$, and that its wave-fronts take the form of a helix advancing in the propagation direction, as can be seen in Figures 1.2 and 1.5.

If the spin contribution were considered in the current analysis, a term corresponding to the polarization of light field will be added to the numerator of Eq. 1.21, and both contributions to optical angular momentum will be separated. It has been shown that beyond the paraxial approximation a theory of angular momentum of light can be developed [53]. However, the separation cannot be achieved from a general non-paraxial beam based on the full Maxwell Theory, nevertheless, the paraxial approximation gives us a simple way to separate the angular momentum into spin and orbital contributions.

1.2.2   Quantum OAM

The quantization of the energy of electromagnetic radiation gave rise to the concept of the photon, from where physicist were able to explain light properties such as energy and momentum from a more fundamental point of view. Even more, this description of light gave rise to several branches in physics, which are contemporary topics with promising applications [54, 55]. The main reason to explain the radiation field in a quantum description, and so the quantum point of view of OAM, was to find a fundamental theory of the nature of this property.

Using the cross product of $\vec{r}$ with Eq. 1.18 and integrating all over the space, one finds that the angular momentum of the classical electromagnetic field can be separated in two

parts [19]:

$$\vec{L}_\perp = \epsilon_0 \sum_i \int d^3\vec{r} E_{i\perp}(\vec{r} \times \nabla) A_{i\perp}, \tag{1.22}$$

$$\vec{S}_\perp = \epsilon_0 \int d^3\vec{r} \vec{E}_\perp \times \vec{A}_\perp, \tag{1.23}$$

here $\vec{A}_\perp$ is the transverse vector potential of the field. The above expressions are the gauge-invariant versions of the original separation of angular momentum, i.e. has a physical interpretation. Trickily the separation of the angular momentum has already been written with L and S, however, no distinction has been made between the extrinsic and intrinsic angular momentum of the field, not even in the early section; one way to define each expression is by comparing with the definitions of classical mechanics. In order to make an analogy to the separation of the total angular momentum of a system of matter particles in external and internal parts (orbital and spin parts), one can observe that Eq. 1.23 is independent to the definition of the origin of the coordinate system, so we consider this expression as the intrinsic part of the angular momentum, and we are now able to call it the spin contribution, leaving Eq. 1.22 as the orbital contribution.

The transverse electromagnetic field can be quantized by expanding the fields in any complete set of transverse vector mode functions that represents the state of the radiation field. The vectors that compose the earlier expression became operators acting in the Hilbert space. Even more; by taking the paraxial approximation it is found that the vector potential, (now an operator $\hat{A}$) can be written in terms of the LG mode annihilation operator [18]

$$\hat{a}_{l,n}(k_0) = \int d^2\vec{q} LG_{l,n}(\vec{q})\hat{a}(\vec{q}, k_0), \tag{1.24}$$

by means that its operation acts as an annihilation of a photon in a Laguerre-Gauss Fock state, and the result of the LG Fock creation operator acting on the vacuum is defined as

$$|L_{l,n}\rangle \equiv \hat{a}_{l,n}^\dagger(k_0) |0\rangle, \tag{1.25}$$

which represents a Laguerre-Gauss mode in a single-photon number state. In the space representation

$$\langle x|L_{l,n}\rangle = \sqrt{\frac{2n!}{\pi(n+|l|)!}} \frac{1}{\omega} \left(\frac{r\sqrt{2}}{\omega}\right)^{|l|} \exp\left(\frac{-r^2}{\omega^2}\right) L_n^{|l|}\left(\frac{2r^2}{\omega^2}\right) \exp(il\phi), \tag{1.26}$$

which is the same as in Eq. 1.9 considering the case $z = 0$.

Since the paraxial OAM and Spin operators are based on $\hat{A}$ (as seen classically in Eq. 1.23

and Eq. 1.22), also can be written in terms of Eq. 1.24; performing this substitution, the field operator of OAM is now

$$\hat{L}_z = \hbar \sum_{l,n} l \int dk_0 \hat{a}^\dagger_{l,n}(k_0) \hat{a}_{l,n}(k_0). \tag{1.27}$$

Given the form of the field operator of OAM given by Eq. 1.27, the Laguerre-Gauss Fock states given by Eq.1.25 are then eigenvectors of the OAM operator, and so the LG Fock states constitute a natural basis for the OAM

$$\mathbb{L} \equiv \langle L_{l,n} | \hat{L}_z | L_{l,n} \rangle = \hbar l. \tag{1.28}$$

This can be understood as that a single-photon in a Laguerre-Gauss mode has well-defined OAM, given by the azimuthal integer number l.

With this analysis in the paraxial regime, one can see that the most general paraxial one-photon state can be described as superpositions of eigenstates of $\hat{L}_z$, that is $|L_{l,n}\rangle$, and so any modal Fock state that is linearly dependent of this quantum state can also describe a paraxial one-photon state.

In order to connect this quantum analysis with the classic case; we use the well-known relation of the magnitude of the momentum of a photon

$$\mathbb{P} = \hbar k_z, \tag{1.29}$$

and calculate the ratio of total angular momentum and energy per photon

$$\frac{\mathbb{L}}{c\mathbb{P}} = \frac{l}{\omega}, \tag{1.30}$$

which is, as it was pointed out before, equitable to Eq. 1.21, and as in the classical case, the OAM is a direct consequence that a mode of light has an azimuthal dependence of $e^{il\phi}$. As l can take any integer value for Orbital Angular Momentum, then, the state space is unbounded.

The operator given by Eq. 1.27 does not obey the commutation relations for the components of angular momentum [56], so rotations on the field cannot be generated, and therefore it does not represent angular momentum, as it is known in a quantum mechanical sense. However, it has been shown that this angular momentum of the radiation field can be transferred to matter so only the components along the propagation direction can

be measured by detecting the change in internal and external angular momentum of matter. So even if the light does not carry angular momentum in the strict quantum physical meaning, it can be transferred to matter in order to generate truly angular momentum.

If the spatial mode of the photon is not an LG mode, it is still possible to calculate the OAM that the photon carries; a simple way to perform this is to express the modal Fock state of interest in terms of the eigenvectors of OAM. In our case, one can express the HIG Fock states in terms of LG Fock states, due to the direct correspondence between the paraxial approximation and the quantum physics representation. These states can be defined as superpositions of even and odd Ince-Gauss Fock states as in the classical case (Eq. 1.17) [30]

$$\left| I_{p,m}^{\pm,\epsilon} \right\rangle = \frac{1}{\sqrt{2}} (\left| I_{p,m}^{e,\epsilon} \right\rangle \pm i \left| I_{p,m}^{o,\epsilon} \right\rangle). \tag{1.31}$$

These even and odd quantum modal states $\left| I_{p,m}^{\sigma,\epsilon} \right\rangle$ can be represented, as in Eq.1.15, as a superposition of even and odd Laguerre-Gauss Fock states

$$\left| I_{p,m}^{e,\epsilon} \right\rangle = \sum_{l,n} D_{ln}^{e}(\epsilon) \left| L_{l,n}^{e} \right\rangle, \tag{1.32}$$

$$\left| I_{p,m}^{o,\epsilon} \right\rangle = \sum_{l,n} D_{ln}^{o}(\epsilon) \left| L_{l,n}^{o} \right\rangle, \tag{1.33}$$

and with Eq. 1.32 and Eq. 1.33, the state given by Eq. 1.31 can be written as

$$\left| I_{p,m}^{\pm,\epsilon} \right\rangle = \frac{1}{\sqrt{2}} \sum_{l,n} \left(D_{ln}^{e}(\epsilon) \left| L_{l,n}^{e} \right\rangle \pm i D_{ln}^{o}(\epsilon) \left| L_{l,n}^{o} \right\rangle \right), \tag{1.34}$$

where D_{ln}^{σ} are the weights of the Laguerre-Gauss expansion, the same as in Eq. 1.16.

Similarly to the the Helical Ince-Gauss modes case, the Laguerre-Gauss Fock states can also be written in terms of even and odd Laguerre- Gauss Fock states as

$$\left| L_{l,n} \right\rangle = \frac{1}{\sqrt{2}} (\left| L_{l,n}^{e} \right\rangle + i \left| L_{l,n}^{o} \right\rangle), \tag{1.35}$$

$$\left| L_{-l,n} \right\rangle = \frac{1}{\sqrt{2}} (\left| L_{l,n}^{e} \right\rangle - i \left| L_{l,n}^{o} \right\rangle), \tag{1.36}$$

where

$$\left\langle x \middle| L_{l,n}^{e,o} \right\rangle = \sqrt{\frac{4n!}{(1+\delta_{0,l})\pi(n+l)!}} \frac{1}{\omega} \left(\frac{r\sqrt{2}}{\omega} \right)^{l} e^{\frac{-r^2}{\omega^2}} L_{n}^{l} \left(\frac{2r^2}{\omega^2} \right) \begin{bmatrix} \cos(l\phi) \\ \sin(l\phi) \end{bmatrix}, \tag{1.37}$$

which are the same as in Eq. 1.11, for the case $z = 0$.

Using the previous expressions is possible to express Eq. 1.31 in terms of Eq. 1.35 and Eq. 1.36, and by considering the correspondence Eq. 1.28 one can obtain the expectation value of OAM for a Helical Ince-Gauss Fock state [30]

$$\langle I_{p,m}^{\pm,\epsilon}| \hat{L}_z |I_{p,m}^{\pm,\epsilon}\rangle = \pm \sum_{n,l} \hbar l D_{ln}^e(\epsilon) D_{ln}^o(\epsilon), \tag{1.38}$$

there is no integer part of the OAM per photon, giving place to fractional expectation values of OAM, that evolves with the ellipticity, which is implicit in Eq. 1.31. This is exemplified in Fig. 1.7 for different HIG Fock states. As it can be seen, the OAM of the HIG modes for $\epsilon \to 0$ is equal to the value of m, since indices relations to the LG modes are $m = l$ and $p = 2n + l$. As the ellipticity grows the OAM of each mode takes fractional values, and as $\epsilon \to \infty$ the OAM tends to an stable value of OAM, which is different for every mode, which shows that the Hermite-Gaussian modes also carries fractional OAM. The intersections of the lines in Fig. 1.7 shows that, with certain ellipticity, exist distinct HIG modes with the same amount of OAM.

An important conclusion of the present section is given by Eq. 1.38; as we pointed out before, every paraxial one-photon state can be described in a complete basis of spatial modes, nevertheless, not every modal Fock state has the same amount of OAM, in fact, as it is possible to approximate the Helical Ince-Gauss modes to Laguerre-Gauss modes and to Helical Hermite-Gauss modes through ellipticity, then, the Eq. 1.38 represents how the OAM evolves from the LG modes to the HG modes, starting from its expected integer value Eq. 1.28.

(a) Even p and m values.

(b) Odd p and m values.
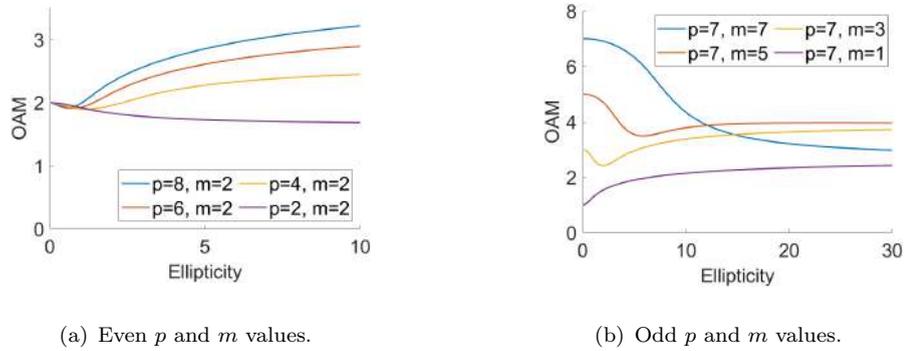
FIGURE 1.7: Expectation value of OAM divided by $\hbar$, for helical Ince-Gauss mode in a single-photon number state.

1.3 Spontaneous Parametric Down-Conversion

In this section we discuss how entangled modal states can be generated experimentally, by the Spontaneous Parametric Down-Conversion process [15]. This process occurs when a high-energy photon enters a nonlinear crystal, then it interacts with the crystal lattice, which creates two lower-energy photons.

The original photon has a frequency of ω and generates two new photons with frequencies of ω_1 and ω_2 such that $\omega = \omega_1 + \omega_2$. If both photons have the same polarization, this process is known as type I SPDC. But if the photon-pair have different polarization, then the process is known as type II SPDC. These two photons are known as the signal and idler photons, and they are entangled with each other in several degrees of freedom, like polarization, frequency, and OAM. This means that their quantum states are correlated in a way that cannot be explained by classical physics. A schematic of the SPDC process is depicted in Fig. 1.8.
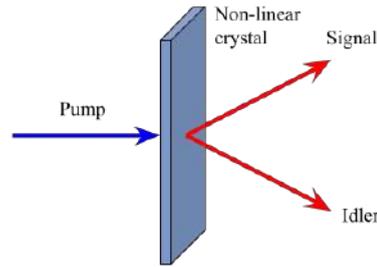
FIGURE 1.8: An SPDC scheme with the Type I output

1.3.1 SPDC Photon-pair Entangled State in LG basis

The signal and idler SPDC photons carry OAM (l_s, l_i) as a consequence of its conservation in the SPDC process. In fact, the OAM that the down-converted photons carry must sum the OAM of the pump photon l_p

$$l_p = l_s + l_i. \tag{1.39}$$

As we discuss in section 1.2.2, the LG Fock states are the natural basis for the OAM given by Eq. 1.28, so if both photons are entangled given the OAM conservation, we should be able to write the quantum state of the OAM of this photons as a superposition of products of these LG spatial modes of the electromagnetic field [16]. Such superposition should be infinite, since the possibilities for l_s and l_i in Eq. 1.39 are also infinite. Such state represents an increase in the dimension of the Hilbert space, in contrast with polarization entangled

states, as it can be as large as l indices are taken, therefore, its richness in quantum information is the subject of current research because of its potential applications for quantum cryptography [23], and quantum computing [57]. Then the emitted photon-pair entangled state, generated by SPDC, is represented by [16]

$$|\Psi\rangle = \sum_{l=0}^{\infty} \sum_{n} C_{n,n}^{l,-l} \left[|L_{l,n}\rangle_A |L_{-l,n}\rangle_B + |L_{-l,n}\rangle_A |L_{l,n}\rangle_B \right], \tag{1.40}$$

here, in particular and without loss of generality, it has been taken the case $l_p = 0$ and $n_p = n_s \equiv n$. The sub-index A and B stand for Alice and Bob, which names refer to the receivers of the photons.

From the state given by Eq. 1.40 the coefficients $|C_{n,n}^{l,-l}|^2$ represents the probability of finding one photon in state $|L_{l,n}\rangle$ and the other in the state $|L_{-l,n}\rangle$; this function represents the OAM spectrum of the state, and can be calculated by the overlap integral

$$C_{n,n}^{l,-l} =_A \langle L_{l,n}| \ _B \langle L_{-l,n}|\Psi\rangle, \tag{1.41}$$

this integral depends on the phase-matching condition given by characteristic parameters of the non-linear crystal that produces SPDC, the pump beam, and the collinear or nearly collinear emission of the down-converted photons [58, 59]. In the limit of a thin crystal, it is possible to solve this integral analytically [60]

$$C_{n,n}^{l,-l} \propto K_n^{|l|} \frac{(-2\gamma^2)^{|l|}}{(1+2\gamma^2)^{2n+|l|}} \times_2 F_1 \left[\begin{matrix} -n, -n \\ -2n - |l| \end{matrix} ; 1 - 4\gamma^4 \right], \tag{1.42}$$

here $_2F_1$ is the Gauss hypergeometric function, and $K_n^{|l|}$ is a combinatorial coefficient with analytic form and also depends on l and n. As we can see, in this thin crystal limit, the coefficients particularly depend on the ratio $\gamma = \frac{\omega_p}{\omega_{s,i}}$, where ω is the beam width. Fig. 1.9 shows $|C_{n,n}^{l,-l}|^2$ normalized for different γ values.

This state is entangled since the projection onto only one of the photons onto a spatial mode defines the spatial mode in which the other photon is found. For example, if we project the photon pair state of Eq. 1.40 onto Eq. $|L_{5,0}\rangle_B$, we get

$$_B\langle L_{5,0}|\Psi\rangle = C_{0,0}^{5,-5} |L_{-5,0}\rangle_A, \tag{1.43}$$

(a) $\gamma = 1$ (b) $\gamma = 1.5$
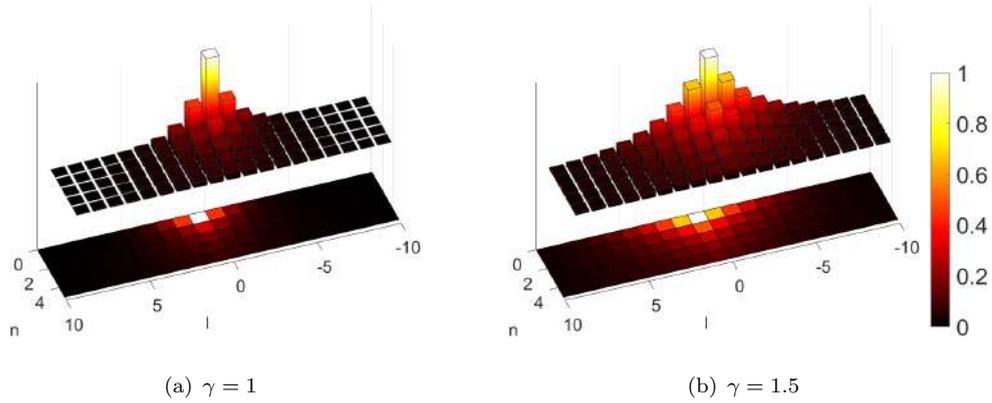
FIGURE 1.9: $|C_{n,n}^{l,-l}|^2$ as a l and n function, for different beam widths, known as OAM Spectrum.

this happens because of the orthogonality condition for the Laguerre-Gauss modes (as in Eq. 1.10)

$$\langle L_{l,n} | L_{l',n'} \rangle = \delta_{ll'} \delta_{nn'}, \tag{1.44}$$

Thus defining the LG quantum state in which the A photon is, removing all other possibilities of state in which the photon could be found. In the next section entanglement is fully explained.

1.4 Entanglement

When two or more quantum particles are entangled, their properties become correlated in such a way that measuring the properties of one particle can instantaneously affect the properties of the other particle, even if they are separated by large distances. This non-local correlation between the entangled particles is a fundamental feature of quantum mechanics and it has been experimentally verified for several quantum states [8, 14, 26, 61–63].

There are several ways to quantify entanglement in quantum systems [2, 3]. One of the most commonly used measures is entropy [64]; this measure is based on the concept of von Neumann entropy, which is a measure of the amount of information contained in a quantum state. Another common quantifier of entanglement is the concurrence [65]; this measure is used to quantify entanglement between two qubits and it is based on the idea of entanglement swapping. These measures are used to quantify the amount of entanglement present in a given quantum state and provide a way to compare the degree of

entanglement between different states or subsystems. They are used to study the properties of entanglement, including its distribution, manipulation, and transformation, and are an essential tool in many areas of quantum information and quantum computing [66, 67]. Most of these measurements require to have a complete knowledge of the density matrix of the system, and this can be achieved by performing precise quantum tomography [68, 69].

As the main objective of this thesis is to explain the HIG modal entanglement of the photon-pair state, given by SPDC, the precise quantum tomography technique is beyond the scope of the work. But in order to confirm the presence of entanglement we use a Bell-type inequality test, which is not a form of quantifying entanglement, but a way of confirming it.

In this section we explain how these tests are performed, measuring the entanglement in superposition states, generally known as qubits. So first we define what a qubit is, then we will define what an entangled state is, thus explaining bell states. And finally, we will discuss what a CHSC-Bell inequality is, and how it can be violated to confirm entanglement.

1.4.1 Qubit

A qubit, short for Quantum bit, is the fundamental unit of quantum information. It is the quantum analogue of a classical bit, which represents the basic unit of classical information and can take on one of two values, 0 or 1. However, unlike classical bits that exist in well-defined states, qubits can exist in a superposition of states, meaning they can simultaneously represent both 0 and 1, or any combination of the two. A qubit can be represented as a two-dimensional vector in a complex vector space, as

$$|\Psi_{qbit}\rangle = \sqrt{a}e^{i\theta}|0\rangle + \sqrt{1-a}e^{-i\theta}|1\rangle, \tag{1.45}$$

here $a \in [0,1]$ and $\theta \in [0,\pi]$. The coefficients described by parameters a and θ, are complex probability amplitudes that determine the probability of measuring the qubit in either state. The normalization condition $|\sqrt{a}e^{i\theta}|^2 + |\sqrt{1-a}e^{-i\theta}|^2 = 1$ ensures that the state is properly normalized.

In Fig. 1.10 the geometric representation of a qubit is shown. This representation is known as the Bloch sphere. It is a unit sphere in three-dimensional space, where each point on the surface of the sphere corresponds to a unique quantum state of the qubit. The sphere's north and south poles represent the two basis states of the qubit, conventionally denoted

as $|0\rangle$ and $|1\rangle$, respectively. The equator of the sphere ($a = 1/2$) represents a superposition of the two basis states, as

$$|\theta\rangle = \frac{1}{\sqrt{2}}(e^{i\theta}|0\rangle + e^{-i\theta}|1\rangle), \tag{1.46}$$
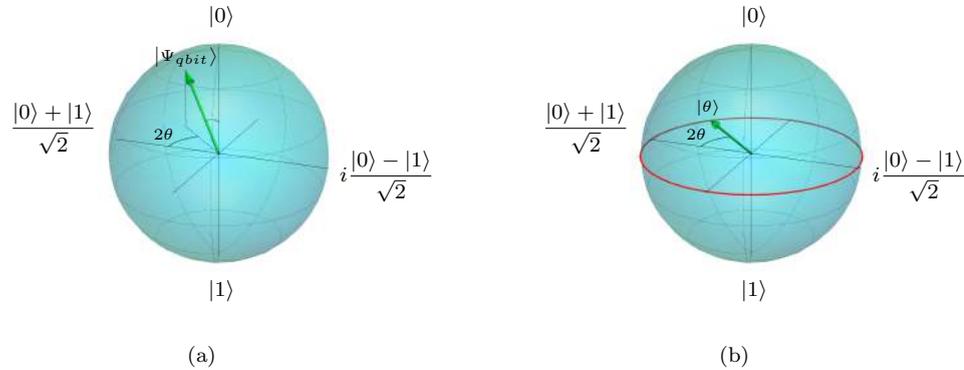
FIGURE 1.10: Bloch sphere

If we multiply a global phase $e^{-i\theta}$ to Eq. 1.46, we get $e^{-i\theta}|\Psi_{qbit}\rangle = \frac{1}{\sqrt{2}}(|0\rangle + e^{-i2\theta}|1\rangle)$, from where we can notice why twice the angle θ represents the azimuth angle of the sphere. This can be done because two qubits with a global phase difference, like $|\Psi_{qbit}\rangle$ and $e^{-i\theta}|\Psi_{qbit}\rangle$, cannot be experimentally distinguished.

Qubits can be physically realized using various quantum systems, such as atoms, ions, photons, superconducting circuits, or even topological properties of certain materials. These physical implementations provide a means to manipulate and measure the quantum states of qubits, allowing for practical applications of quantum information processing.

1.4.2 Bell states

Entanglement is a phenomenon where the state of a composite quantum system cannot be described as a product of the states of its individual subsystems. In other words, the quantum state of the composite system cannot be written as a tensor product of the states of its constituent subsystems [1]. This phenomenon is a consequence of the superposition principle in quantum mechanics, where particles can exist in multiple states simultaneously. When two or more particles become entangled, their combined state cannot be described as a simple combination of the individual states of each particle. Instead, their states are described by a joint quantum state that encompasses all possible configurations.

The Bell states, also known as EPR pairs (Einstein-Podolsky-Rosen pairs), are a set of four maximally entangled quantum states [2]

$$\left|\Phi^+\right\rangle = \frac{1}{\sqrt{2}}\left(\left|0\right\rangle_A\left|1\right\rangle_B + \left|1\right\rangle_A\left|0\right\rangle_B\right), \tag{1.47}$$

$$\left|\Phi^-\right\rangle = \frac{1}{\sqrt{2}}\left(\left|0\right\rangle_A\left|1\right\rangle_B - \left|1\right\rangle_A\left|0\right\rangle_B\right), \tag{1.48}$$

$$\left|\Psi^+\right\rangle = \frac{1}{\sqrt{2}}\left(\left|0\right\rangle_A\left|0\right\rangle_B + \left|1\right\rangle_A\left|1\right\rangle_B\right), \tag{1.49}$$

$$\left|\Psi^-\right\rangle = \frac{1}{\sqrt{2}}\left(\left|0\right\rangle_A\left|0\right\rangle_B - \left|1\right\rangle_A\left|1\right\rangle_B\right). \tag{1.50}$$

Here, we used the computational basis $|0\rangle$ and $|1\rangle$, that fulfill orthogonality: $\langle 0|1\rangle = \langle 1|0\rangle = 0$ and $\langle 0|0\rangle = \langle 1|1\rangle = 1$.

This states are maximally entangled because they cannot be factored into separate states, and represent states of the highest possible degree of entanglement between two qubits. Measurement outcomes on one particle are instantaneously correlated with the measurement outcomes on the other particle, regardless of the spatial separation between them.

1.4.3 CHSH-Bell inequality

The CHSH-Bell inequality is a mathematical inequality formulated for binary measurements, where the outcomes of the measurements are represented by binary values [7]. This inequality is satisfied by any local hidden variable theory, which is a class of theories that assume that the properties of a system are determined by pre-existing values that are hidden from observation. If the CHSH-Bell inequality is violated, it means that the correlations of the system are stronger than what can be explained by local realistic theories. Instead, the results suggest that quantum mechanics is the correct theory to describe the system [3].

There are three main conditions in order to use the CHSH-Bell inequality; first, this inequality is designed to assess the correlations between measurements performed on entangled particles, so we need an entangled system. Second, it assumes that the measurements performed on the entangled particles have two possible outcomes. Lastly, the inequality assumes that the measurement settings are chosen independently for each particle. This is to ensure that the measurements are not coordinated or influenced in a way that could violate the principles of local realism. The Bell states meet these three conditions.

The entangled particles are denoted by particle a and particle b. As we have two entangled particles, we need to measure the correlations between them with two detectors, each detector will have two detection settings, which are denoted by A, A' for the first detector, and B, B' for the second one. With this, the CHSH-Bell inequality can be written as [3, 14]

$$S = |E(A, B) - E(A, B') + E(A', B) + E(A', B')| \leq 2, \tag{1.51}$$

here S is known as the Bell parameter, and $E(A, B)$ is the correlation between the measurements of A and B on photon a and photon b, respectively, and similarly for the other terms. The correlation is defined as the probability that the results of the measurements are the same. If the value of S is greater than 2, then the CHSH-Bell inequality is violated, which means that the predictions of quantum mechanics are not consistent with those of classical physics, and even more, the entanglement is confirmed.

A way to perform a Bell test is by testing the entanglement in different bases than in which the system is entangled. We can do this with a superposition state of the entangled states, in particular, we can perform the Bell test by measuring the correlations with a qubit. Thus the angles of Eq. 1.46 works as the detector settings for the measurements, such as $A = \theta_A$, $A' = \theta'_A$, $B = \theta_B$ and $B' = \theta'_B$ [14, 26]. With this, we can obtain the correlation function $E(\theta_A, \theta_B)$, with the joint probability $C(\theta_A, \theta_B)$, which is the probability of detecting one photon in the state $|\theta_A\rangle$ and the other is $|\theta_B\rangle$

$$E(\theta_A, \theta_B) =$$
$$\frac{C(\theta_A, \theta_B) + C(\theta_A + \pi/2, \theta_B + \pi/2) - C(\theta_A + \pi/2, \theta_B) - C(\theta_A, \theta_B + \pi/2)}{C(\theta_A, \theta_B) + C(\theta_A + \pi/2, \theta_B + \pi/2) + C(\theta_A + \pi/2, \theta_B) + C(\theta_A, \theta_B + \pi/2)}. \tag{1.52}$$

We can calculate the angles that maximize S for each Bell state, but as will be shown in the following sections, only states $|\Psi^+\rangle$ of Eq. 1.47 and $|\Phi^+\rangle$ of Eq. 1.49 will be of interest.

Projecting the states $|\theta_A\rangle$ and $|\theta_B\rangle$, on the state $|\Psi^+\rangle$, and squaring its absolute value [14]

$$C(\theta_A, \theta_B) = |\langle\theta_A|\langle\theta_B|\Psi^+\rangle|^2 = \left|\frac{1}{2}\left[e^{i(\theta_B - \theta_A)} + e^{-i(\theta_B - \theta_A)}\right]\right|^2, \tag{1.53}$$

$$C(\theta_A, \theta_B) = \cos^2(\theta_B - \theta_A). \tag{1.54}$$

Substituting this into $E(\theta_A, \theta_B)$ given by Eq.1.52, and then in S given by Eq. 1.51 we are able to find a set of angles that maximize the CHSH-Bell inequality to $S = 2\sqrt{2}$. The set of angles that maximize S for the state $|\Psi^+\rangle$ are $\theta_A = 0°$, $\theta_B = 22.5°$, $\theta'_A = 45°$, $\theta'_B = 67.5°$.

Now, projecting the states $|\theta_A\rangle$ and $|\theta_B\rangle$, on the state $|\Phi^+\rangle$, and squaring its absolute value

$$C(\theta_A, \theta_B) = |\langle\theta_A|\langle\theta_B|\Phi^+\rangle|^2 = \left|\frac{1}{2}\left[e^{i(\theta_B+\theta_A)} + e^{-i(\theta_B+\theta_A)}\right]\right|^2, \tag{1.55}$$

$$C(\theta_A, \theta_B) = \cos^2(\theta_B + \theta_A). \tag{1.56}$$

Similarly to the previous case, we now obtain a set of angles that maximize the Bell parameter to $S = 2\sqrt{2}$, for the state $|\Phi^+\rangle$, which are $\theta_A = 90°$, $\theta_B = 22.5°$, $\theta'_A = 45°$, $\theta'_B = 67.5°$.

It is noteworthy that the set of angles that maximize the Bell parameter for the state $|\Psi^+\rangle$ are the angles from where a minimum of S is found for the state $|\Phi^+\rangle$, and vice versa. So by using the correct set of angles, it is possible to confirm the entanglement of each state.

Chapter 2

Entangled State of Spontaneous Parametric Down Conversion in a Helical Ince-Gauss Basis

We delve into the derivation of a comprehensive theoretical framework for describing the entangled state generated by Spontaneous Parametric Down Conversion in the Helical Ince-Gauss basis. This chapter serves as a crucial foundation for understanding the unique characteristics and properties of the SPDC state in the description of helical Ince-Gauss modes.

Throughout this chapter, we will use not only all the mathematical techniques of the previous chapter; such as mode expansion, quantum field theory, and operator algebra. But to derive a change of basis of the entangled state provided by the SPDC, to a Helical Ince-Gauss basis, we will need some definitions about how the HIG states can be described as superposition states and as entangled states.

We discuss the implications of this description. Mainly, we explain how the quantum state behaves when varying the ellipticity parameter of the basis, and explain how is it possible to confirm the entanglement of such state in a experiment.

By developing a theoretical framework that describes the SPDC state in the Helical Ince-Gauss basis, we provide a tool for analyzing and manipulating entangled state of photon pairs generated through SPDC processes. This chapter lays the groundwork for subsequent investigations in understanding the behavior of the SPDC state in helical Ince-Gauss modes.

2.1 Representation of the HIG states

Here we define some necessary states, with which we can not only make the change of basis of the entangled state, given by SPDC, in terms of HIG modes, but also to be able to confirm entanglement by means of a Bell inequality.

2.1.1 HIG Bloch Sphere

As our entanglement modal test, is a direct analogy to the entanglement given via polarization [8, 70], we need to define a Bloch sphere for spatial modes, as is shown in Fig. 2.1. As in section 1.4.1, any point on the sphere can be represented by

$$|\Psi\rangle = \sqrt{a}e^{i\theta}\left|I_{p,m}^{+,\epsilon}\right\rangle + \sqrt{1-a}e^{-i\theta}\left|I_{p,m}^{-,\epsilon}\right\rangle, \tag{2.1}$$

as in Eq. 1.45.

The poles of the sphere are HIG modes, and each point on the equator represents a specific superposition with a well-defined phase and can be represented by [31]

$$|\theta\rangle = \frac{1}{\sqrt{2}}\left(e^{i\theta}\left|I_{p,m}^{+,\epsilon}\right\rangle + e^{-i\theta}\left|I_{p,m}^{-,\epsilon}\right\rangle\right), \tag{2.2}$$

as in Eq. 1.46.
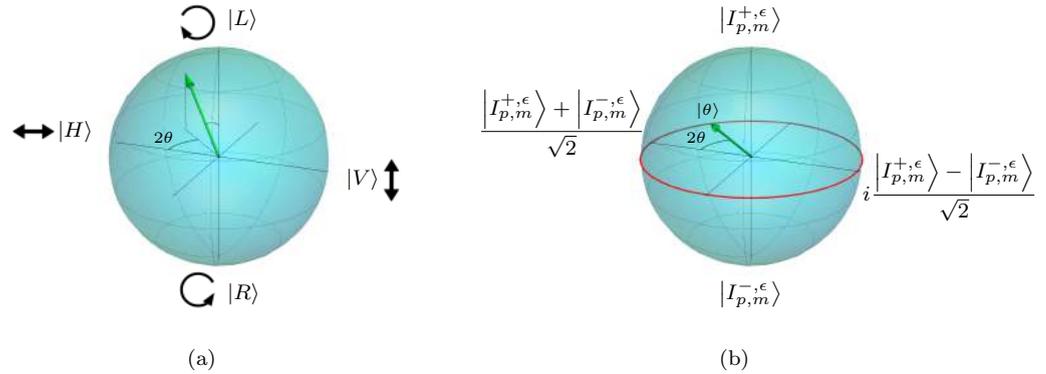
FIGURE 2.1: Bloch sphere constructed from a) polarization and b) Helical Ince-Gauss modes

We will take as an example the quantum numbers $p = 6$, $m = 2$ and $\epsilon = 3$, to show the Bloch sphere constructed from the Ince-Gauss modes. In Fig. 2.2 the Bloch sphere is shown. The insets in the figure display the intensity pattern with its corresponding phase

pattern. The intensity patterns at the north and south poles are indistinguishable. While a continuous phase change of θ along the equator, these patterns also undergo continuous shape changes.
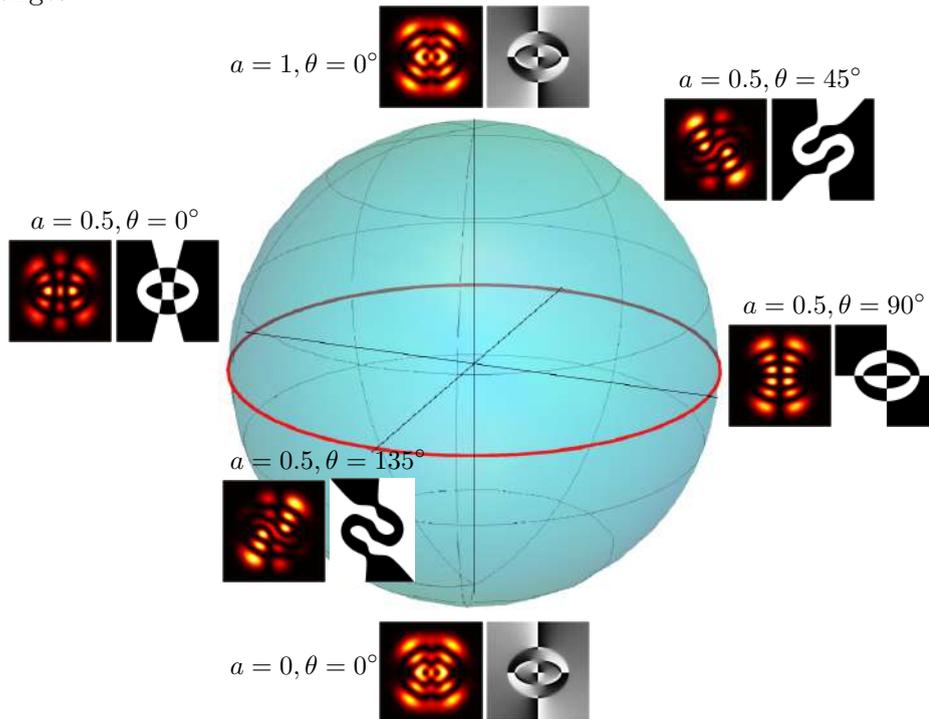
FIGURE 2.2: Bloch sphere constructed from $p = 6$, $m = 2$ and $\epsilon = 3$.

2.1.2 HIG Bell States

It is possible to describe analogous Bell states in other bases than the standard computational basis ($|0\rangle$ and $|1\rangle$ basis). The standard Bell test involves measuring the entangled qubits in the computational basis to test for the violation of certain correlations predicted by quantum mechanics. However, by choosing different measurement bases, one can investigate different aspects of entanglement and test different correlations.

As in subsection 1.4.2, we define the HIG Bell states as

$$\left|\Phi^+\right\rangle = \frac{1}{\sqrt{2}} \left(\left|I_{p,m}^{+,\epsilon_A}\right\rangle_A \left|I_{p,m}^{+,\epsilon_B}\right\rangle_B + \left|I_{p,m}^{-,\epsilon_A}\right\rangle_A \left|I_{p,m}^{-,\epsilon_B}\right\rangle_B \right), \tag{2.3}$$

$$\left|\Phi^-\right\rangle = \frac{1}{\sqrt{2}} \left(\left|I_{p,m}^{+,\epsilon_A}\right\rangle_A \left|I_{p,m}^{+,\epsilon_B}\right\rangle_B - \left|I_{p,m}^{-,\epsilon_A}\right\rangle_A \left|I_{p,m}^{-,\epsilon_B}\right\rangle_B \right), \tag{2.4}$$

$$\left|\Psi^+\right\rangle = \frac{1}{\sqrt{2}} \left(\left|I_{p,m}^{+,\epsilon_A}\right\rangle_A \left|I_{p,m}^{-,\epsilon_B}\right\rangle_B + \left|I_{p,m}^{-,\epsilon_A}\right\rangle_A \left|I_{p,m}^{+,\epsilon_B}\right\rangle_B \right), \tag{2.5}$$

$$|\Psi^-\rangle = \frac{1}{\sqrt{2}}\left(\left|I_{p,m}^{+,\epsilon_A}\right\rangle_A \left|I_{p,m}^{-,\epsilon_B}\right\rangle_B - \left|I_{p,m}^{-,\epsilon_A}\right\rangle_A \left|I_{p,m}^{+,\epsilon_B}\right\rangle_B\right). \tag{2.6}$$

Hence we have defined the states as sums of products of HIG states with the same numbers p and m, but with distinct ellipticity for each qubit. The latter is possible since the family of IG solutions is orthogonal with respect to indices and parity, but not to ellipticity [28] (as in Eq. 1.14)

$$\left\langle I_{p,m}^{\sigma,\epsilon} \middle| I_{p',m'}^{\sigma',\epsilon'} \right\rangle = \delta_{\sigma\sigma'}\delta_{pp'}\delta_{mm'}. \tag{2.7}$$

It is noteworthy that ellipticity is a characteristic quite unique attributed to these modes, which does not exist for LG modes, and as ϵ is a continuous variable, it can be understood as a non-trivial continuous rotation parameter for the infinite-dimensional basis of the Hilbert space [31].

2.2 SPDC Photon-pair Entangled State in HIG basis

Here we calculate the probability of finding the photon-pair entangled state, generated by SPDC, in Helical Ince-Gauss Fock states, with the same p and m quantum numbers, but different ellipticity.

Given that the Helical Ince-Gauss modes are expanded in the even and odd Laguerre-Gauss modes, it is possible to express Eq. 1.40 in this modes, given Eq. 1.35 and Eq. 1.36, then the photon pair state is

$$\begin{aligned}
|\Psi\rangle = \sum_{l=0}^{\infty}\sum_{n} \frac{C_{n,n}^{l,-l}}{2} &\left[\left(\left|L_{l,n}^e\right\rangle_A + i\left|L_{l,n}^o\right\rangle_A\right)\left(\left|L_{l,n}^e\right\rangle_B - i\left|L_{l,n}^o\right\rangle_B\right)\right.\\
&\left.+ \left(\left|L_{l,n}^e\right\rangle_A - i\left|L_{l,n}^o\right\rangle_A\right)\left(\left|L_{l,n}^e\right\rangle_B + i\left|L_{l,n}^o\right\rangle_B\right)\right],
\end{aligned} \tag{2.8}$$

simplifying this expression, we get

$$|\Psi\rangle = \sum_{l=0}^{\infty}\sum_{n} C_{n,n}^{l,-l}[\left|L_{l,n}^e\right\rangle_A \left|L_{l,n}^e\right\rangle_B + \left|L_{l,n}^o\right\rangle_A \left|L_{l,n}^o\right\rangle_B]. \tag{2.9}$$

Now it can be easily derived the desired probabilities. First, we calculate the probability of finding the photon-pair state in a HIG Fock state, both with the same quantum numbers p, m, with distinct helicity. Lastly we calculate the same joint probability, but with equal helicity.

2.2.1 Different Helicity Probability

First, the projection of Eq. 2.9 with the state $\left|I_{p,m}^{+,\epsilon_A}\right\rangle_A$ is

$$_A\langle I_{p,m}^{+,\epsilon_A}|\Psi\rangle = \frac{1}{\sqrt{2}}\left(\sum_{l,n} D_{ln}^e(\epsilon_A)\left\langle L_{l,n}^e\right|_A - i\sum_{l,n} D_{ln}^o(\epsilon_A)\left\langle L_{l,n}^o\right|_A\right)|\Psi\rangle. \tag{2.10}$$

On substituting this on Eq. 2.9

$$_A\langle I_{p,m}^{+,\epsilon_A}|\Psi\rangle = \frac{\sqrt{2}}{2}\sum_{n,l} C_{n,n}^{l,-l}[D_{ln}^e(\epsilon_A)\left|L_{l,n}^e\right\rangle_B - iD_{ln}^o(\epsilon_A)\left|L_{l,n}^o\right\rangle_B]. \tag{2.11}$$

Now the projection of $\left|I_{p,m}^{-,\epsilon_B}\right\rangle_B$ in the above equation is

$$_B\langle I_{p,m}^{-,\epsilon_B}|\,_A\langle I_{p,m}^{+,\epsilon_A}|\Psi\rangle = \frac{1}{2}\sum_{n,l} C_{n,n}^{l,-l}[D_{ln}^e(\epsilon_A)D_{ln}^e(\epsilon_B) + D_{ln}^o(\epsilon_A)D_{ln}^o(\epsilon_B)], \tag{2.12}$$

which is the same for the projection in the states $\left|I_{p,m}^{-,\epsilon_A}\right\rangle_A\left|I_{p,m}^{+,\epsilon_B}\right\rangle_B$. This is the modal HIG amplitude probability, and its squared absolute value is the modal HIG amplitude probability, which is the probability of finding the photon-pair state in a specific HIG Fock state with modal numbers p, m and ϵ_A for photon A, and ϵ_B for photon B, both with distinct helicity.

There are two main characteristics of this probability that have to be highlighted:

First, as the quantum numbers increase, the modal probability decreases for values $\epsilon_A \neq \epsilon_B$. This happens because as ϵ_A take values far from ϵ_B, the coefficients $D_{ln}^\sigma(\epsilon_A)$ and $D_{ln}^\sigma(\epsilon_B)$ tend to be more and more distinct from each other, such as $D_{ln}^\sigma(\epsilon_A) < D_{ln}^\sigma(\epsilon_B)$, and the products given in Eq. 2.12 are smaller than in the $\epsilon_A = \epsilon_B$ case. This behavior is stronger for greater values of p, as the terms of the sum on Eq. 2.12 increase with this number. This is shown in Fig. 2.3 a), b) and c), where the normalized squared absolute value of Eq. 2.12 is shown for $p = 3, m = 1$, $p = 8, m = 6$ and $p = 15, m = 9$ as a function of the ellipticities (ϵ_A, ϵ_B) for $\gamma = 1.5$ (The experimental value of γ). In order to show how the probability decreases when $\epsilon_A \neq \epsilon_B$ for higher quantum numbers, Figures 2.3 d), e) and f) shows the normalized contour lines for some fixed ϵ_A of the squared absolute value of Eq. 2.12, given by the red, blue and yellow lines in Figures 2.3 a), b) and c), corresponding to $\epsilon_A = 2, 5, 9$ correspondingly. The probability as an ϵ function gets narrower for higher modes.

(a) $_B\left\langle I_{3,1}^{-,\epsilon_B}\right|{}_A\left\langle I_{3,1}^{+,\epsilon_A}\middle|\Psi\right\rangle$ (b) $_B\left\langle I_{8,6}^{-,\epsilon_B}\right|{}_A\left\langle I_{8,6}^{+,\epsilon_A}\middle|\Psi\right\rangle$ (c) $_B\left\langle I_{15,9}^{-,\epsilon_B}\right|{}_A\left\langle I_{15,9}^{+,\epsilon_A}\middle|\Psi\right\rangle$

(d) Contour lines for fixed ϵ_A, and $p = 3$, $m = 1$.   (e) Contour lines for fixed ϵ_A, and $p = 8$, $m = 6$.   (f) Contour lines for fixed ϵ_A, and $p = 15$, $m = 9$.
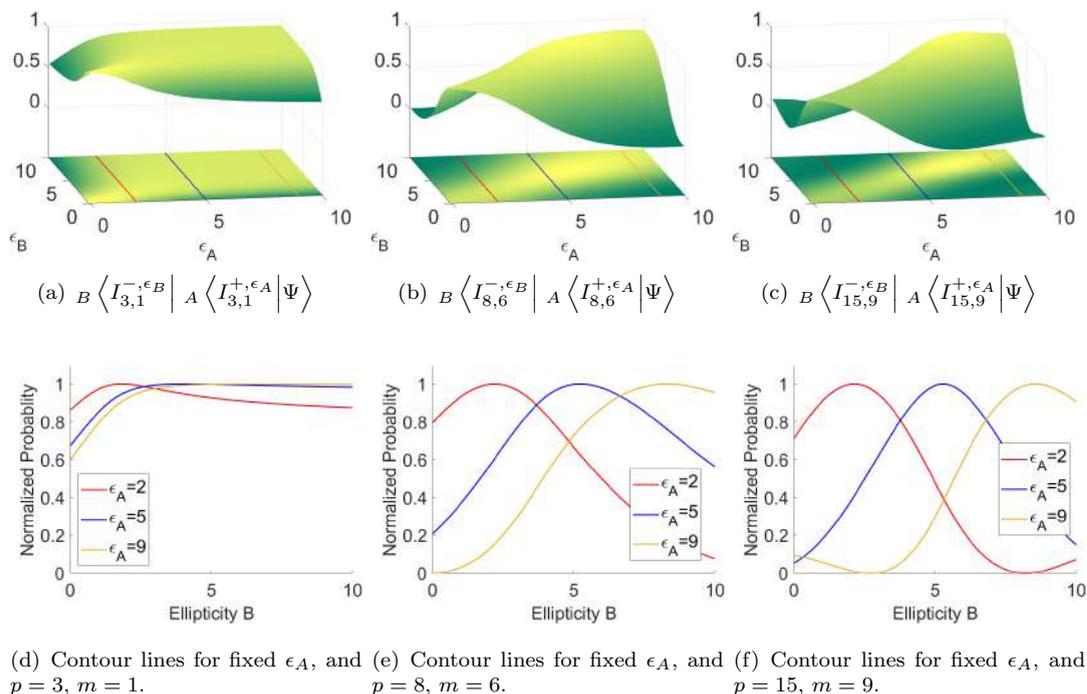
FIGURE 2.3: Normalized probabilities $_B\left\langle I_{p,m}^{-,\epsilon_B}\right|{}_A\left\langle I_{p,m}^{+,\epsilon_A}\middle|\Psi\right\rangle$ from low to high order modes.

The second main characteristic of Eq. 2.12, is that the probability reaches its maximum value when $\epsilon_A = \epsilon_B \equiv \epsilon_{AB}$, having a global maximum in some specific ϵ_{AB}, which varies depending on the HIG mode. For modes with the lowest m value, for a given p, the probability for ϵ_{AB} monotonically decreases; this decay becomes more pronounced for higher m modes. On the other hand, for modes with the highest m value, for a given p, the probability for ϵ_{AB} monotonically increases. This general behavior of the probability as an ellipticity function, is attributed to the SPDC's OAM spectrum; as the $C_{n,n}^{l,-l}$ coefficients limit the products of the $D_{ln}(\epsilon_{AB})$ coefficients in Eq. 2.12, which endows this characteristic that prefers certain values ϵ_{AB} with which the maximum probability is found. This can be seen in Fig. 2.4, where the normalized squared absolute value of Eq. 2.12 is shown for fixed $p = 17$ and $m = 5, 7, 9$, as an (ϵ_A, ϵ_B) function with $\gamma = 1.5$. Fig. 2.4 d), e) and f) shows the normalized contour lines for the squared absolute value of Eq. 2.12 for ϵ_{AB}, corresponding to the diagonal lines in Figures 2.4 a), b) and c). Table 2.1 shows the ϵ_{AB} value at which the maximum probability is reached for these modes.

In Fig. 2.5, the normalized squared absolute value of Eq. 2.12 is shown, contrary to the previous case, for $p = 12, 14, 16$ and fixed $m = 6$, as an (ϵ_A, ϵ_B) function with $\gamma = 1.5$. Fig. 2.5 d), e) and f) shows the normalized contour lines for the squared absolute value of

(a) $\left| {}_B \left\langle I_{17,5}^{-,\epsilon_B} \right| {}_A \left\langle I_{17,5}^{+,\epsilon_A} \middle| \Psi \right\rangle \right.$

(b) ${}_B \left\langle I_{17,7}^{-,\epsilon_B} \right| {}_A \left\langle I_{17,7}^{+,\epsilon_A} \middle| \Psi \right\rangle$

(c) ${}_B \left\langle I_{17,9}^{-,\epsilon_B} \right| {}_A \left\langle I_{17,9}^{+,\epsilon_A} \middle| \Psi \right\rangle$

(d) Contour line $\epsilon_A = \epsilon_B$ for mode $p = 17, m = 5$

(e) Contour line $\epsilon_A = \epsilon_B$ for mode $p = 17, m = 7$

(f) Contour line $\epsilon_A = \epsilon_B$ for mode $p = 17, m = 9$
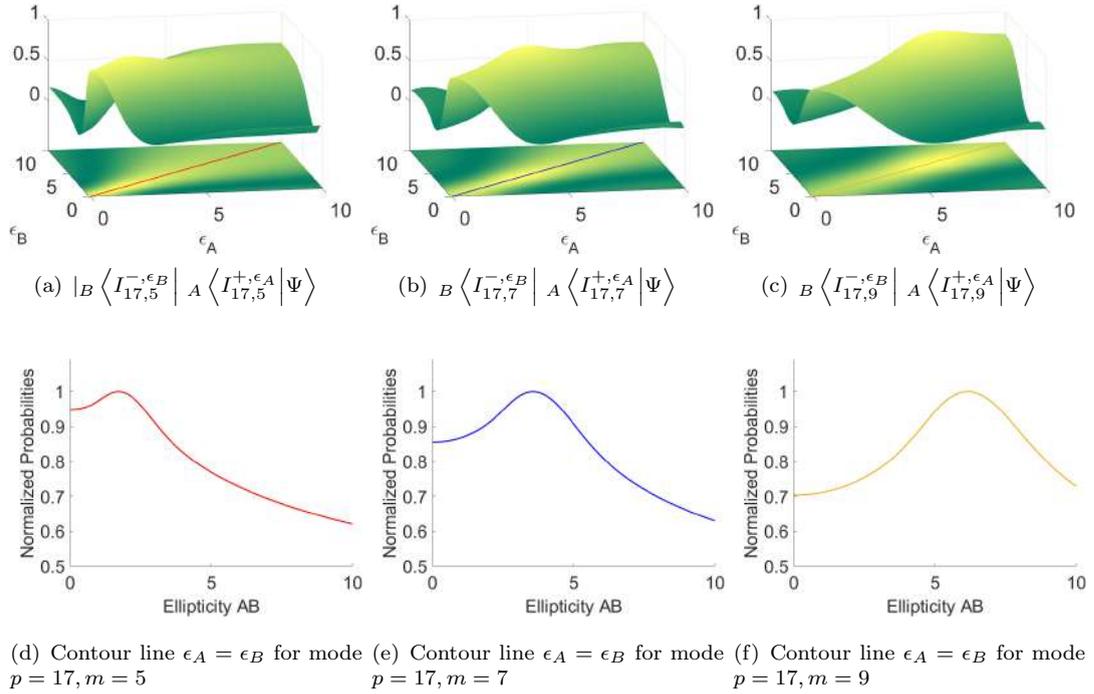
FIGURE 2.4: Normalized probabilities ${}_B \left\langle I_{p,m}^{-,\epsilon_B} \right| {}_A \left\langle I_{p,m}^{+,\epsilon_A} \middle| \Psi \right\rangle$ and different m values.

TABLE 2.1: Maximum ellipticity values for the different helicity case, for fixed p.

HIG Quantum Numbers	$p = 17, m = 5$	$p = 17, m = 7$	$p = 17, m = 9$
ϵ_{AB}	1.7	3.6	6.2

Eq. 2.12 for ϵ_{AB}, corresponding to the diagonal lines in Figures 2.5 a), b) and c). Table 2.2 shows the ϵ_{AB} value at which the maximum probability is reached for these modes.

TABLE 2.2: Maximum ellipticity values for the different helicity case, for fixed m.

HIG Quantum Numbers	$p = 12, m = 6$	$p = 14, m = 6$	$p = 16, m = 6$
ϵ_{AB}	3.6	3.0	2.6

As it is shown in Table 2.1, if we fix the modal number p, the ϵ_{AB} value, that maximizes the joint probability given by Eq. 2.12, increases along with m. On the contrary, as it

(a) $_B\left\langle I_{12,6}^{-,\epsilon_B}\right|\,_A\left\langle I_{12,6}^{+,\epsilon_A}\middle|\Psi\right\rangle$

(b) $_B\left\langle I_{14,6}^{-,\epsilon_B}\right|\,_A\left\langle I_{14,6}^{+,\epsilon_A}\middle|\Psi\right\rangle$

(c) $_B\left\langle I_{16,6}^{-,\epsilon_B}\right|\,_A\left\langle I_{16,6}^{+,\epsilon_A}\middle|\Psi\right\rangle$

(d) Contour line $\epsilon_A = \epsilon_B$ for mode $p = 12, m = 6$.

(e) Contour line $\epsilon_A = \epsilon_B$ for mode $p = 14, m = 6$.

(f) Contour line $\epsilon_A = \epsilon_B$ for mode $p = 16, m = 6$.
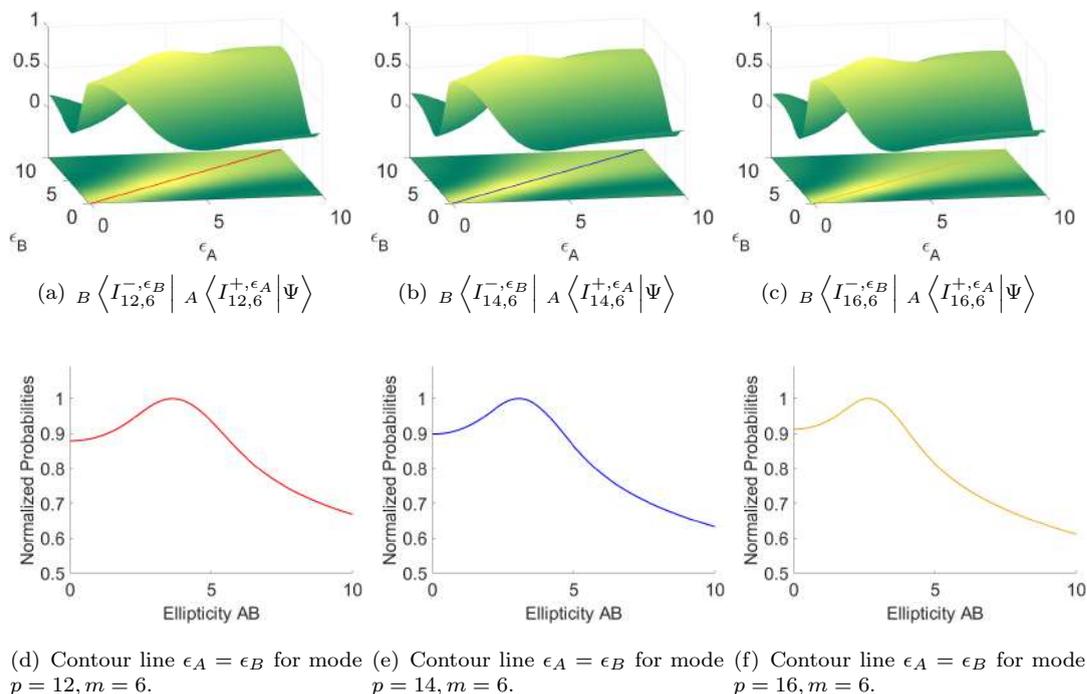
FIGURE 2.5: Normalized probabilities $_B\left\langle I_{p,m}^{-,\epsilon_B}\right|\,_A\left\langle I_{p,m}^{+,\epsilon_A}\middle|\Psi\right\rangle$ and different p values.

is shown in Table 2.2, if we fix the modal number m, the ϵ_{AB} value, that maximizes the joint probability given by Eq. 2.12, decreases when the modal number p increases.

From Figures 2.3, 2.4 and 2.5, it is clear that the mode probabilities of photon-pair entangled state, given by the SPDC, change with ϵ_A and ϵ_B, which means that the probability of finding this state, in a specific HIG mode can be tuned with the ellipticity values. Since the entanglement of SPDC photon-pair state is given via OAM conservation, the probability tuning should not come as a surprise, as in the earlier section it was established that the OAM of a stable beam may be tuned by adjusting the ellipticity value. We can take advantage of this continuous parameter in order to find which ϵ_{AB} value maximize the probability of finding any HIG mode in this quantum state.

2.2.2 Same Helicity Probability

We just calculated the probability of finding both photons with distinct helicity, analogously to the state described in LG Fock states. In the same way, we can also calculate the probability of finding both photons in HIG states with the same helicity for both photons. The projection of Eq. 2.9 with the states $\left|I_{p,m}^{+,\epsilon_A}\right\rangle_A \left|I_{p,m}^{+,\epsilon_B}\right\rangle_B$, given by Eq. 1.34, will provide the probability amplitude of finding the photon-pair state in the positive Helical

Ince-Gaussian state

$$_B\langle I_{p,m}^{+,\epsilon_B}| \; _A\langle I_{p,m}^{+,\epsilon_A}|\Psi\rangle = \frac{1}{2}\sum_{n,l} C_{n,n}^{l,-l}[D_{ln}^e(\epsilon_A)D_{ln}^e(\epsilon_B) - D_{ln}^o(\epsilon_A)D_{ln}^o(\epsilon_B)], \qquad (2.13)$$

which is the same for the projection in the states $\left|I_{p,m}^-\right\rangle_A \left|I_{p,m}^-\right\rangle_B$. As it is shown, in the Ince-Gassuian base the photon-pair entangled state does not behave as in the Laguerre-Gaussian basis. In the Laguerre-Gaussian case the expectation value of finding both photons with the same helicity in the state is null, but in the Ince-Gaussian base the probability of finding both photons with the same helicity does not vanish, this is due that the expansion coefficients for the Ince-Gauss beams differs for the different parities $D_{ln}^e \neq D_{ln}^o$, except in the limit $\epsilon \to 0$, where we recover the zero probability as we are in the Laguerre-Gauss case. This is shown in Fig. 2.6, where the squared absolute value of Eq. 2.13 is shown for the same modes as in Fig. 2.4 (fixed $p = 17$ and $m = 5, 7, 9$), as an (ϵ_A, ϵ_B) function with $\gamma = 1.5$. Figures 2.6 a), b) and c) shows the contour lines for the squared absolute value of Eq. 2.13 from where a maximum value of the probability is found for some fixed ϵ_A, corresponding to the red, blue and yellow lines in Figures 2.6 d), e) and f). Table 2.3 shows the ϵ_{AB} value at which the maximum probability is reached for these modes.

(a) $_B\left\langle I_{17,5}^{+,\epsilon_B}\right| \; _A\left\langle I_{17,5}^{+,\epsilon_A}|\Psi\right\rangle$ (b) $_B\left\langle I_{17,7}^{+,\epsilon_B}\right| \; _A\left\langle I_{17,7}^{+,\epsilon_A}|\Psi\right\rangle$ (c) $_B\left\langle I_{17,9}^{+,\epsilon_B}\right| \; _A\left\langle I_{17,9}^{+,\epsilon_A}|\Psi\right\rangle$

(d) Contour line for fixed ϵ_A, and $p = 17$, $m = 5$.   (e) Contour line for fixed ϵ_A, and $p = 17$, $m = 7$.   (f) Contour line for fixed ϵ_A, and $p = 17$, $m = 9$.
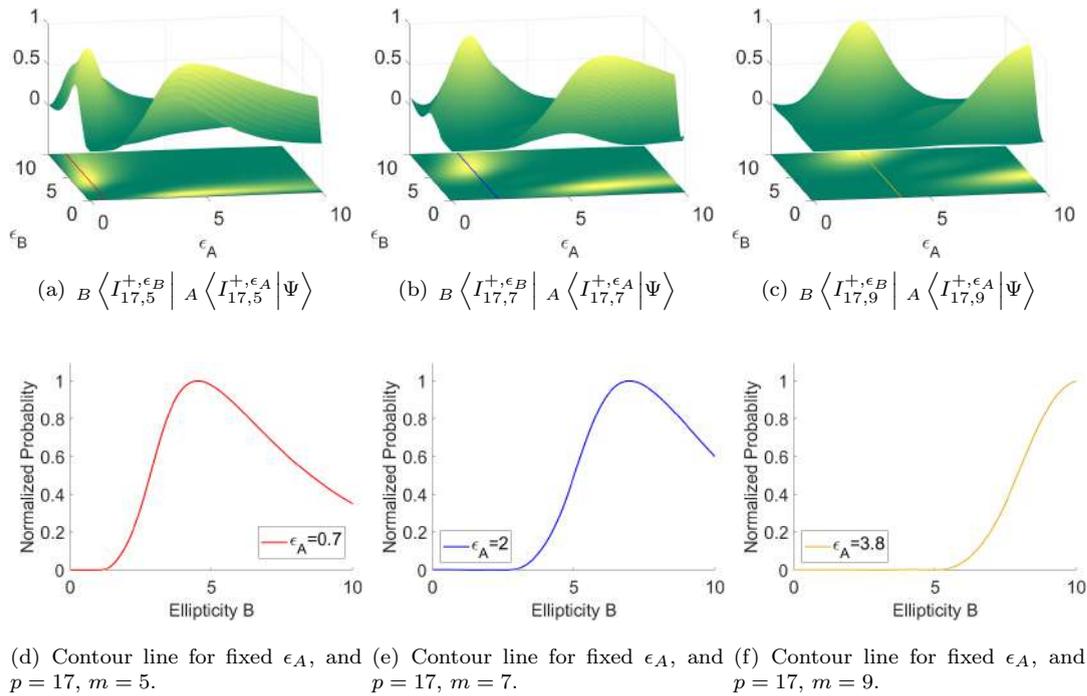
FIGURE 2.6: Normalized probabilities $_B\left\langle I_{p,m}^{+,\epsilon_B}\right| \; _A\left\langle I_{p,m}^{+,\epsilon_A}|\Psi\right\rangle$ for different modes.

TABLE 2.3: Maximum ellipticity values for the same helicity case, for fixed p.

HIG Quantum Numbers	$p = 17, m = 5$	$p = 17, m = 7$	$p = 17, m = 9$
ϵ_A	0.7	2.0	3.8
ϵ_B	4.5	7.0	9.9

In Fig. 2.7, where the squared absolute value of Eq. 2.13 is shown for the same modes as in Fig. 2.5 ($p = 12, 14, 16$ and $m = 6$), as an (ϵ_A, ϵ_B) function with $\gamma = 1.5$. Figures 2.7 a), b) and c) shows the contour lines for the squared absolute value of Eq. 2.13 from where a maximum value of the probability is found for some fixed ϵ_A, corresponding to the red, blue and yellow lines in Figures 2.6 d), e) and f). Table 2.22 shows the ϵ_{AB} value at which the maximum probability is reached for these modes.

(a) $_B\left\langle I_{12,6}^{+,\epsilon_B}\right| {}_A\left\langle I_{12,6}^{+,\epsilon_A}\middle|\Psi\right\rangle$ (b) $_B\left\langle I_{14,6}^{+,\epsilon_B}\right| {}_A\left\langle I_{14,6}^{+,\epsilon_A}\middle|\Psi\right\rangle$ (c) $_B\left\langle I_{16,6}^{+,\epsilon_B}\right| {}_A\left\langle I_{16,6}^{+,\epsilon_A}\middle|\Psi\right\rangle$

(d) Contour line for fixed ϵ_A, and $p = 12$, $m = 6$.   (e) Contour line for fixed ϵ_A, and $p = 14$, $m = 6$.   (f) Contour line for fixed ϵ_A, and $p = 16$, $m = 6$.
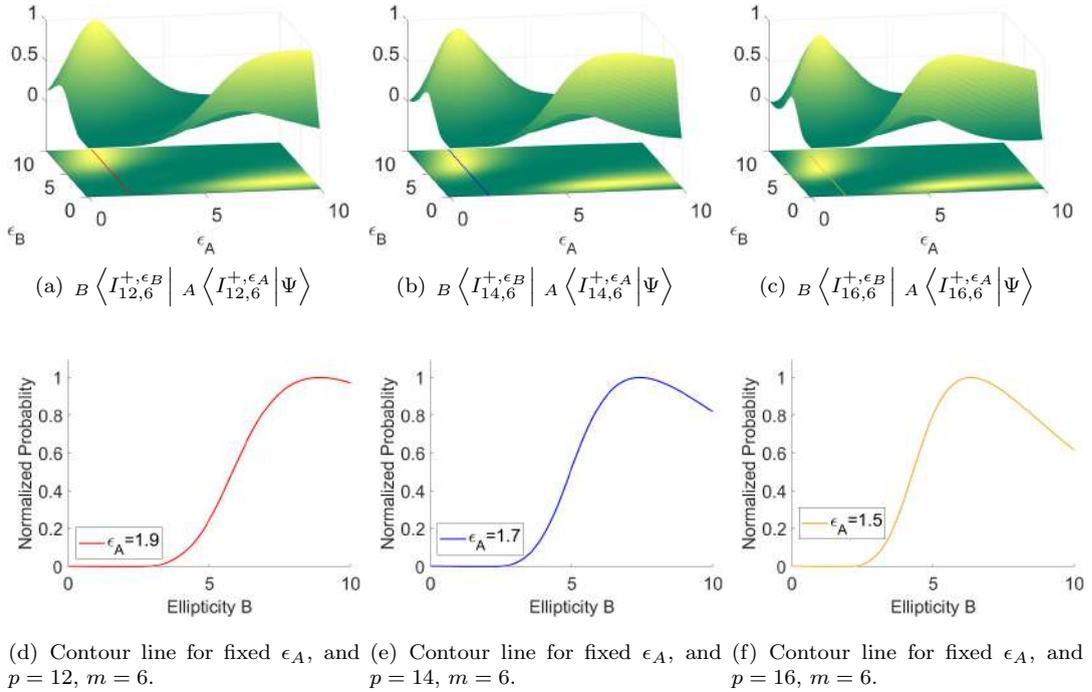
FIGURE 2.7: Normalized probabilities $_B\left\langle I_{p,m}^{+,\epsilon_B}\right| {}_A\left\langle I_{p,m}^{+,\epsilon_A}\middle|\Psi\right\rangle$ for different modes.

The ellipticity values that maximizes the probability of finding both photons with the same helicity, changes with the modal numbers p and m, in the same manner than in the contrary case. As it is shown in Table 2.3, if we fix the modal number p, the ϵ_A and ϵ_B values, that maximizes the joint probability given by Eq. 2.13, increases along with m.

TABLE 2.4: Maximum ellipticity values for the same helicity case, for fixed m.

HIG Quantum Numbers	$p = 12, m = 6$	$p = 14, m = 6$	$p = 16, m = 6$
ϵ_A	1.9	1.7	1.5
ϵ_B	8.9	7.4	6.3

On the contrary, as it is shown in Table 2.4, if we fix the modal number m, the ϵ_A and ϵ_B values, that maximizes the joint probability given by Eq. 2.13, decreases when the modal number p increases.

The ellipticity values that maximize the probability of finding both photons with equal helicity are the same values that minimize the opposite case, this is shown in Fig. 2.8, where the normalized probabilities are depicted. This occurs for the same reasons as in the different helicity case; when the coefficients $D_{ln}(\epsilon_A)$ and $D_{ln}(\epsilon_B)$ tend to be more and more distinct from each other (when the ϵ_A value is far from ϵ_B), the products given in Eq. 2.13 are greater than the $\epsilon_A = \epsilon_B$ case, because of the minus sign.

(a) $|F_{5,3}|^2$ (b) $|F_{11,5}|^2$ (c) $|F_{17,7}|^2$

(d) $|G_{5,3}|^2$ (e) $|G_{11,5}|^2$ (f) $|G_{17,7}|^2$
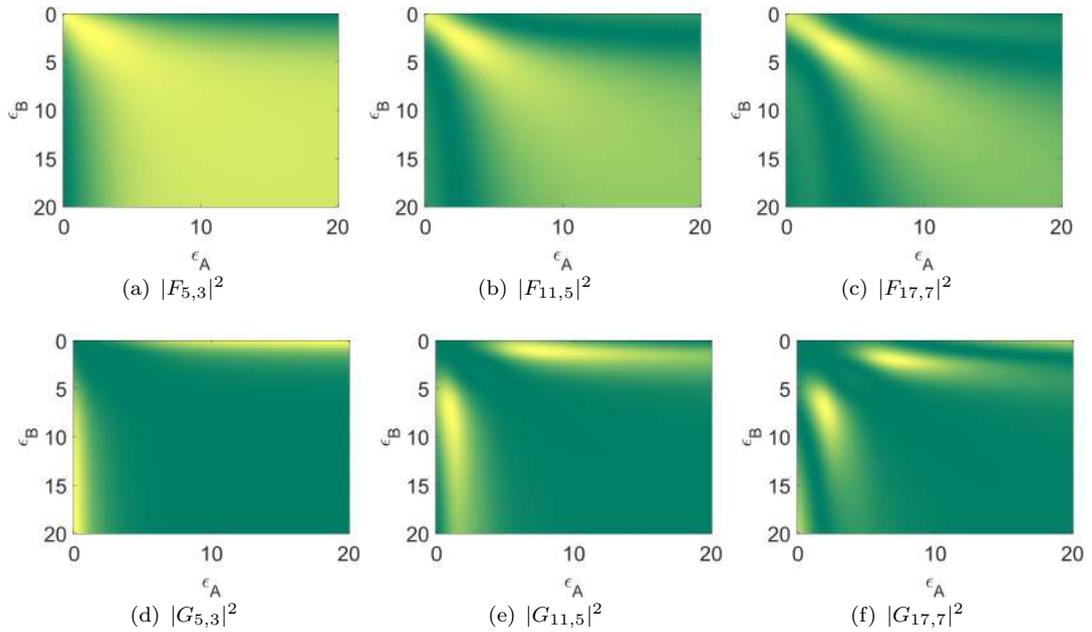
FIGURE 2.8: Normalized $|F_{p,m}|^2$ and $|G_{p,m}|^2$ coefficients.

2.2.3 Entangled State

From this analysis, we finally arrived at the main characteristic of this photon-pair state, generated by SPDC, on HIG basis. As the HIG modes describes a complete family solution to the Paraxial Wave Equation, and given the direct correspondence between the paraxial approximation and the quantum physics representation, we have calculated not only the amplitude probabilities, but a change of basis of the photon-pair state, generated by SPDC, in terms of the HIG Fock states.

Given Eq. 2.12 and Eq. 2.13, we can consider this quantum state as a sum of two infinite sums of symmetric HIG Bell-states in the form of

$$
\begin{aligned}
|\Psi\rangle = \sum_{p,m} F_{p,m} & \left[\left|I_{p,m}^{+,\epsilon_A}\right\rangle_A \left|I_{p,m}^{-,\epsilon_B}\right\rangle_B + \left|I_{p,m}^{-,\epsilon_A}\right\rangle_A \left|I_{p,m}^{+,\epsilon_B}\right\rangle_B \right] + \\
\sum_{p,m} G_{p,m} & \left[\left|I_{p,m}^{+,\epsilon_A}\right\rangle_A \left|I_{p,m}^{+,\epsilon_B}\right\rangle_B + \left|I_{p,m}^{-,\epsilon_A}\right\rangle_A \left|I_{p,m}^{-,\epsilon_B}\right\rangle_B \right],
\end{aligned}
\tag{2.14}
$$

with the $F_{p,m}$ and $G_{p,m}$ coefficients as

$$
F_{p,m} = \frac{1}{2} \sum_{n,l} C_{n,n}^{l,-l} [D_{ln}^e(\epsilon_A) D_{ln}^e(\epsilon_B) + D_{ln}^o(\epsilon_A) D_{ln}^o(\epsilon_B)],
\tag{2.15}
$$

$$
G_{p,m} = \frac{1}{2} \sum_{n,l} C_{n,n}^{l,-l} [D_{ln}^e(\epsilon_A) D_{ln}^e(\epsilon_B) - D_{ln}^o(\epsilon_A) D_{ln}^o(\epsilon_B)],
\tag{2.16}
$$

which, for some p and m values, are truncated by the D_{ln}^σ terms, such that $p = 2n+l$, then, the number of terms is given by the value of p, having a total of $p - \lceil \frac{p}{2} \rceil + 1$ terms. It is also noteworthy that when $\epsilon_{A,B} \to 0$ then $G_{p,m} \to 0$, $F_{p,m} \to \sum_{n,l} C_{n,n}^{l,-l}$ and $\left|I_{p,m}^{\pm,\epsilon}\right\rangle \to |L_{\pm l,n}\rangle$, and the photon-pair entangled state in the OAM basis of Eq. 1.40 is recovered.

As we will see in the next subsection, an entangled state requires that the state be a non-factorable state, and so the joint state of the system cannot be factored into the product of the individual states. At first sight the state Eq. 2.14 seems to not fit on this entangled state definition, as it can be factored on individual states. But as we discuss earlier, for some HIG mode with some p, m and by choosing the correct ellipticity values, it is possible to maximize the coefficient $F_{p,m}$, thus minimizing $G_{p,m}$, and in this case we can approximate the state to

$$
|\Psi^+\rangle \approx \frac{1}{\sqrt{2}} \left(\left|I_{p,m}^{+,\epsilon_A}\right\rangle_A \left|I_{p,m}^{-,\epsilon_B}\right\rangle_B + \left|I_{p,m}^{-,\epsilon_A}\right\rangle_A \left|I_{p,m}^{+,\epsilon_B}\right\rangle_B \right),
\tag{2.17}
$$

on the contrary, for some p, m and by choosing the correct ellipticity values, it is possible to maximize the coefficient $G_{p,m}$, which will minimize $F_{p,m}$, approximating the state to

$$|\Phi^+\rangle \approx \frac{1}{\sqrt{2}} \left(\left|I_{p,m}^{+,\epsilon_A}\right\rangle_A \left|I_{p,m}^{+,\epsilon_B}\right\rangle_B + \left|I_{p,m}^{-,\epsilon_A}\right\rangle_A \left|I_{p,m}^{-,\epsilon_B}\right\rangle_B \right). \qquad (2.18)$$

Thereby, by varying the ellipticity it is not only possible to tune the probability of finding the photon-pair state in a specific HIG Bell-state, but also, for a particular value of p and m, it is possible to choose a different Bell state, with different symmetry. This is made, by only finding which value of ϵ_A and ϵ_B maximize either Eq. 2.15 or Eq. 2.16. This depends on the desired case.

Even if there is a probability of finding both down-converted photons in IG modes with equal helicity, the maximum value for $|F_{p,m}|^2$ is greater than $|G_{p,m}|^2$ for any p and m values, this is not depicted in Fig. 2.8 as every graph is normalized by its own maximum value. In table 2.5 a direct comparison for some p and m values is shown.

TABLE 2.5: Comparison of the maximum probability values

	$p = 5, m = 3$	$p = 11, m = 5$	$p = 17, m = 7$
$|F_{p,m}|^2_{max}/|G_{p,m}|^2_{max}$	8.29	14.11	19.27

2.3 Entanglement

The SPDC Photon-pair Entangled State in a HIG basis, as described in Eq. 2.14, is a superposition of two HIG Bell states, of different weights. And considering that we can tune such weights by tuning the ellipticity value of the base. We will test the modal entanglement of the state by performing a Bell test, with the CHSH-Bell inequality.

2.3.1 CHSH-Bell inequality for SPDC Photon-pair Entangled State in HIG basis

We calculate the expected value S for the photon-pair state, given by SPDC Eq. 2.9, with the superposition states $|\theta_A\rangle$ and $|\theta_B\rangle$ given by Eq. 2.2. In order to do this it will be convenient to write Eq. 2.2 in terms of the even and odd Laguerre-Gauss quantum modes,

by using Eq. 1.34

$$|\theta\rangle = \frac{1}{2}e^{i\theta}\left(\sum_{l,n}D_{ln}^{e}(\epsilon)\left|L_{l,n}^{e}\right\rangle + i\sum_{l,n}D_{ln}^{o}(\epsilon)\left|L_{l,n}^{o}\right\rangle\right)$$
$$+\frac{1}{2}e^{-i\theta}\left(\sum_{l,n}D_{ln}^{e}(\epsilon)\left|L_{l,n}^{e}\right\rangle - i\sum_{l,n}D_{ln}^{o}(\epsilon)\left|L_{l,n}^{o}\right\rangle\right), \tag{2.19}$$

by factoring

$$|\theta\rangle = \frac{1}{2}[(e^{i\theta}+e^{-i\theta})\sum_{l,n}D_{ln}^{e}(\epsilon)\left|L_{l,n}^{e}\right\rangle + i(e^{i\theta}-e^{-i\theta})\sum_{l,n}D_{ln}^{o}(\epsilon)\left|L_{l,n}^{o}\right\rangle], \tag{2.20}$$

simplifying we finally get

$$|\theta\rangle = \cos(\theta)\sum_{l,n}D_{ln}^{e}(\epsilon)\left|L_{l,n}^{e}\right\rangle - \sin(\theta)\sum_{l,n}D_{ln}^{o}(\epsilon)\left|L_{l,n}^{o}\right\rangle. \tag{2.21}$$

Projecting this for both photons in Eq. 2.9, we can obtain the joint probability since

$$\langle\theta_B|\Psi\rangle = 2\sum_{l,n}C_{n,n}^{l,-l}[D_{ln}^{e}(\epsilon_B)\cos(\theta_B)\left|L_{l,n}^{e}\right\rangle_A - D_{ln}^{o}(\epsilon_B)\sin(\theta_B)\left|L_{l,n}^{o}\right\rangle_A], \tag{2.22}$$

Then it follows

$$\langle\theta_A|\langle\theta_B|\Psi\rangle = 2\cos(\theta_A)\cos(\theta_B)\sum_{l,n}C_{n,n}^{l,-l}D_{ln}^{e}(\epsilon_A)D_{ln}^{e}(\epsilon_B)$$
$$+2\sin(\theta_A)\sin(\theta_B)\sum_{l,n}C_{n,n}^{l,-l}D_{ln}^{o}(\epsilon_A)D_{ln}^{o}(\epsilon_B), \tag{2.23}$$

Therefore, we get

$$C(\theta_A,\theta_B) = |2\cos(\theta_A)\cos(\theta_B)\sum_{l,n}C_{n,n}^{l,-l}D_{ln}^{e}(\epsilon_A)D_{ln}^{e}(\epsilon_B)$$
$$+2\sin(\theta_A)\sin(\theta_B)\sum_{l,n}C_{n,n}^{l,-l}D_{ln}^{o}(\epsilon_A)D_{ln}^{o}(\epsilon_B)|^2. \tag{2.24}$$

In Fig. 2.9 the value of S given by Eq. 1.51 is shown, by using $E(\theta_A,\theta_B)$ of Eq. 1.52 and $C(\theta_A,\theta_B)$ of Eq. 2.24, with the set of angles that maximize the inequality for the states $|\Psi^+\rangle$ and $|\Phi^+\rangle$.

As it is shown, most of the values for ϵ_A and ϵ_B maximize the Bell parameter S for the case where the entanglement is given by $|\Psi^+\rangle$, which corresponds to the same values that

(a) $\left|\Psi^+\right\rangle$, $p=9$, $m=5$

(b) $\left|\Psi^+\right\rangle$, $p=12$, $m=8$

(c) $\left|\Psi^+\right\rangle$, $p=17$, $m=5$

(d) $\left|\Phi^+\right\rangle$, $p=9$, $m=5$

(e) $\left|\Phi^+\right\rangle$, $p=12$, $m=8$

(f) $\left|\Phi^+\right\rangle$, $p=17$, $m=5$
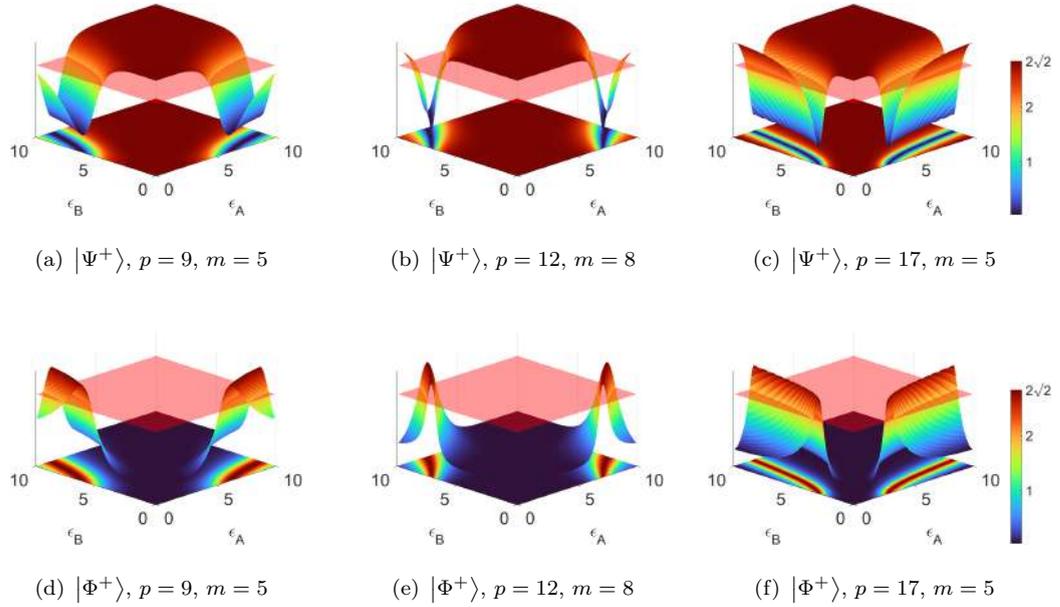
FIGURE 2.9: S value as a function of ϵ_A and ϵ_A for distinct modes. The first row corresponds to angles that maximize the violation of the $\left|\Psi^+\right\rangle$. The second row corresponds to angles that maximize the violation of the $\left|\Phi^+\right\rangle$. The red transparent plane is placed in $S=2$.

maximize the probability of founding such state, the entanglement is given in big areas of ellipticity values. In the case that maximizes inequality for the state $\left|\Phi^+\right\rangle$, there are small regions of values of ellipticity, for which Bell's inequality is violated. However, even if there are fewer values that maximize this case, this still verifies the form of the state given in Eq. 2.14.

Chapter 3

Experimental Realization

We seek to demonstrate that the probability of finding the photon-pair state of the SPDC in HIG modes, can really be tuned with the ellipticity parameter, and even more that it behaves as predicted by Eq. 2.15 and Eq. 2.16. We do this by experimentally measuring the contour lines as in figures 2.3, 2.4 and 2.6. In order to do that, we build a source of pairs of entangled photons by SPDC.

Once we have our source of photon pairs, we need to measure how many photons of the SPDC beam exist in this HIG states. To do this, first, we need to project the state into the HIG modes, we can do it by transforming all the photons that are in this spatial mode into Gaussian modes, this is easily done with a Spatial Light Modulator.

If the photons are in a Gaussian mode we can couple them into a Single mode fiber and count them, in a certain exposure time, the incoming photons that arrive within a coincidence window small enough to ensure that we are detecting photons from the same pair. This coincidence counts will provide us with the probability of the state, since this is proportional to the joint probabilities given by the square of the modulus of the corresponding coefficient in the state vector, in this case by Eq. 2.15 and Eq. 2.16.

Throughout this chapter, each part of the experimental process is described in detail, making special emphasis on how it is possible to perform the projection of the modes, in the state provided by the SPDC process, through the Spatial Light Modulator.

3.1 Spatial Light Modulation

It is possible to modify the amplitude, phase, or polarization of light waves at different points in space, this technique is called spatial light modulation and this is typically achieved using an optical device called a Spatial Light Modulator (SLM), which can control the optical properties of light by manipulating the transmission or reflection of light at various spatial points, so by using it, we can convert a Gaussian mode into another optical beam with a well defined complex amplitude such as Laguerre-Gauss, Hermite-Gauss and as the present case, the Helical Ince-Gauss modes. SLMs are widely used in many different applications, including microscopy [71], holography [72], optical communication [73], and optical computing [74].

One common type of SLM is based on liquid crystal technology. In this type of SLM, an array of liquid crystal pixels is right between two transparent electrodes. When a voltage is applied to an individual pixel, the liquid crystal molecules in that pixel reorient, which changes the phase of the light passing through it.

In the experiment, we use a HOLO EYE Pluto SLM with a 1920 x 1080 pixel display, with each pixel size of 8 μm. This is connected to a computer via HDMI, so we display on it the phase pattern of an IG mode with a specific ellipticity. The display of the SLM reads the green channel of the computer images, and each specific value of the grey level of the display converts it into a phase difference, this relation between the phase and the grey scale was experimentally done in our group and it is showed in Fig. 3.1. With the experimental data we were able to fit the polynomial curve $f(x) = 50.4 + 71.1x + 55.7x^2 + 3.13x^3 - 23.4x^4 + 5.75x^5 - 2.22x^6$ in order to facilitate the relationship between the desired hologram phase and the necessary grey level in the MATLAB code.

3.1.1 Projection in Ince-Gauss Modes

To measure a photon in a Helical Ince-Gauss mode, we need to transfer to it the opposite amount of OAM so its wavefront becomes a Gaussian mode, once the photon carries no OAM it is possible to couple it into a Single Mode Fiber (SMF) and only then we can count the incoming photons. To do this we use the method presented by Bentley *et al.* [75].

We can write the HIG given by Eq. 1.17 in terms of its amplitude and phase in cartesian coordinates as

$$HIG_{p,m}^{\pm}(\vec{r}, \epsilon) = M(x,y)e^{i\phi(x,y)} \tag{3.1}$$
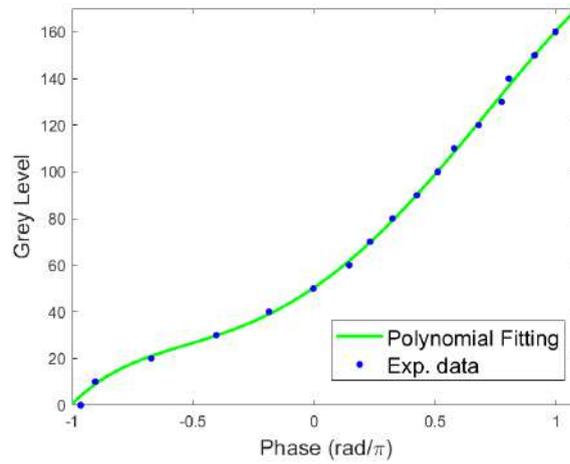
FIGURE 3.1: Gamma Curve Characterization

To create the desired beam we take advantage of the hologram technique; here a interference pattern is computationally created with a reference Gaussian wave and our desired wave (HIG modes), this pattern is displayed in the SLM, so when illuminated by a Gaussian wave it is converted into the desired beam, and as was previously mentioned it works in reverse. This hologram can be easily created by adding to the mode phase a linear phase grating with a d period

$$M(x,y)e^{i[\phi(x,y)+2\pi x/d]} \tag{3.2}$$

The total phase of Eq. 3.2 is the desired mask and to use it in the SLM we use the grey scale presented in Eq. 3.1. An example of this method for the mode $p = 6$, $m = 2$ is shown in Fig. 3.2.

(a) $|HIG_{6,2}^+(\vec{r},4)|^2$

(b) $HIG_{6,2}^+(\vec{r},4)$ phase

(c) Linear phase added to $HIG_{6,2}^+(\vec{r},4)$ phase

FIGURE 3.2: Generation of helical Ince–Gaussian beams with a Spatial Light Modulator.

The position of these patterns must be well centered with respect to the incident beam, a miss-position of these masks cause undesirable projections of superposition modes, to

make sure it is well centered we use an image system with a CCD camera that allows us to see the SLM plane illuminated by the SPDC beam from where we can ensure that the mask and the beam are centered with each other.

It is possible to encode amplitude information in the SLM by modulating the phase pattern with $M(x, y)$, which allows not only to convert the phase of the Gaussian beam into the Helical Ince-Gauss distribution phase but the intensity pattern can be recreated. This works fine for classical beams, but as the power efficiency of the SLM to convert incident beams is around 20% and this percentage decreases when using this modulating method we cannot afford to lose any more photons from the SPDC beam, since it is already a very inefficient process, so we only use the grating method.

3.1.2 Bell test

In section 1.4.3 it was clarified that in order to confirm the entanglement of our system we can perform a Bell test, for this we proposed the idea of corroborating entanglement with a specific superposition of states that violate Bell's inequality. Thus to obtain the Eq. 1.51 parameter we need to evaluate Eq. 1.52 in four different pairs of angles, and each evaluation consists in measuring count rates at four distinct angles. So in order to obtain the Bell parameter for the SPDC state in a specific IG mode we need 16 coincidence counts measurements.
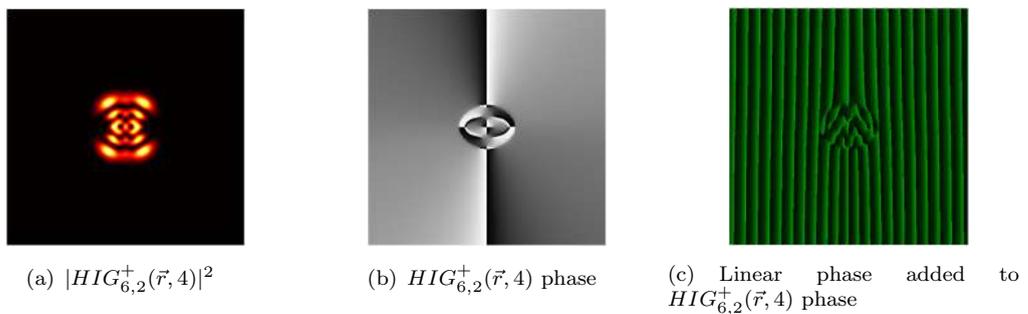
The process to find the parameter is as follows; first, we evaluate the correlation function in one pair of angles, for example, $\theta_A = 173°$ and $\theta_B = 106°$, for this, we need to project each photon in different superposition states which correspond to $|173°\rangle_A$ and $|106°\rangle_B$ and then measure the coincidence counts $C(173°, 106°)$, this states are depicted in Fig. 3.3 for the mode $p = 6, m = 2$.

We repeat the same procedure with a $\pi/2$ displacement in each angle, getting so the other three coincidence counts ($C(263°, 106°)$, $C(173°, 196°)$, $C(263°, 196°)$) necessary to obtain one evaluation in the correlation function $E(173°, 106°)$, given by Eq. 1.52.

3.2 Experimental Arrangement

Fig. 3.4 shows our experimental arrangement. The down-conversion source is a MOGlabs laser with an average output power of 30 mW at 405 nm. The laser beam is coupled to a single-mode fiber in order to select a $l_p = 0$ as the OAM pumping index (this is not shown

(a) Intensity $\theta = 173°$ (b) Phase $\theta = 173°$ (c) Mask $\theta = 173°$

(d) Intensity $\theta = 106°$ (e) Phase $\theta = 106°$ (f) Mask $\theta = 106°$
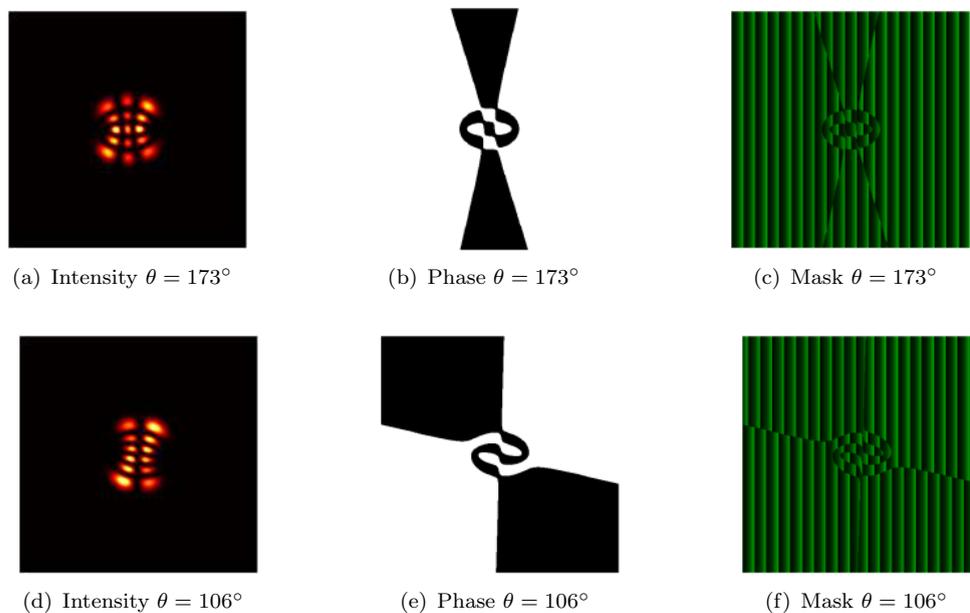
FIGURE 3.3: Superposition modes $e^{i\theta} HIG_{6,2}^{+}(\vec{r}, 4) + e^{-i\theta} HIG_{6,2}^{-}(\vec{r}, 4)$ to measure coincidence counts. The first row is put in the SLM for the A photon, and the last row for the B photon.

in the figure). To build a type-I collinear SPDC source the polarization of the pump beam must be parallel to the extraordinary axis of the non-linear crystal, this is controlled with a half-wave plate. The beam is focused inside the BBO crystal with a lens of $f_0 = 1000$ mm , giving a beam waist at the crystal of $w_0 = 310$ μm. The BBO crystal dimensions are 8 x 8 x 2 mm^3, its optical axis is $\theta_p = 29.2°$ with the surface, and the right incidence angle where the degenerate collinear emission is found can be calculated and estimated experimentally by tilting the optical axis of the crystal. Once the down-converted photons are generated, we get rid of the pump and the non-degenerate photons through a high-pass filter and a band-pass filter centered at 808 nm, with a width of $\Delta\lambda = 10$ nm.

In order to perform photon counting, we need to measure how many photons with the desired spiral phase exists in the beam, to do this we use a Spatial Light Modulator. To improve the efficiency of the projection of a photon with a spiral phase it is necessary to increment the beam size on the Spatial Light Modulator, so the image of the crystal is mapped into a SLM with a magnifier telescope and since we work with the collinear case, we were able to separate the photon pair with a beam splitter right in the middle of this image system. We used a lens of $f_1 = 100$ mm and a pair of lenses of $f_2 = 250$ mm.

The experiment requires modulating both photons with one SLM. This was achieved with the help of a knife edge mirror, since this allows us to put both photons on the SLM display

FIGURE 3.4: Experimental setup.

of small dimensions by directing each photon close to the edge of each face of the KEM with a small angle, this reflects the beam towards the SLM with the same angle, and so the desired diffraction order is recovered into the same face of the KEM with nearly the opposite angle, this diagram is depicted in Fig. 3.5.

FIGURE 3.5: Positioning of the KEM to make both photons fall on a single SLM.

After the photons have passed through the SLM its wavefront becomes a Gaussian mode and then are coupled into single-mode fibers, which are directly connected to avalanche photodiodes to count incoming photons and measure the coincidence count rates in a coincidence window set on 12 ns. To do this, it is necessary to reduce the incoming beam, because of the fiber's core size. This was done with a couple of demagnifier telescopes in each photon path, for this we used four lenses with $f_3 = 250$ mm, $f_4 = 100$ mm, $f_5 = 500$ mm and $f_6 = 8$ mm.

Chapter 4

Results and Discussion

Several modes were measured to confirm the tunable probability given by Eq. 2.15 and Eq. 2.16, we show, in each section, the most suitable modes to show the properties given by the theoretical description. These measurements were taken as discussed in Chapter 3. We measure the coincidence detection of each mode with ellipticity steps of 0.5 from the 0 limit to 10, with an exposure time of 10 s per measure and an average of 10 measurements per ellipticity value taken. In our experimental setup $\gamma = 1.5$, so this value is used in all the theoretical descriptions that uses the coefficient $C_{n,n}^{l,-l}$ given by 1.42, as in chapter 2.

4.1 Probability detection of IG modes with distinct helicity

Modes with low m values generate monotonous growth on the probability function Eq. 2.15, with regard to the ellipticity dependence, while modes with high m values generate monotonous decreases. We show the modes $p = 9, m = 5$, $p = 13, m = 7$ and $p = 15, m = 9$ for the detection probability given by the squared modulus of Eq. 2.15 in Fig. 4.1 a), b) and c). These modes were chosen to show our capability to find experimentally the maximum number of coincidence counts. Figures 4.1 d), e), and f) shows that the experimental results agree with the probability mode detection, specifically, on the range $\epsilon \in (1, 10)$ for the $p = 9$, $m = 5$ mode. On the range $\epsilon \in (2, 10)$ for the $p = 13$, $m = 7$ mode. On the range $\epsilon \in (3, 10)$ for the $p = 13$, $m = 7$ mode. The experimental data finds its maximum value almost in the same values of the theoretical description. Table 4.1 shows the ϵ_{AB} value at which the maximum probability is reached for these modes.
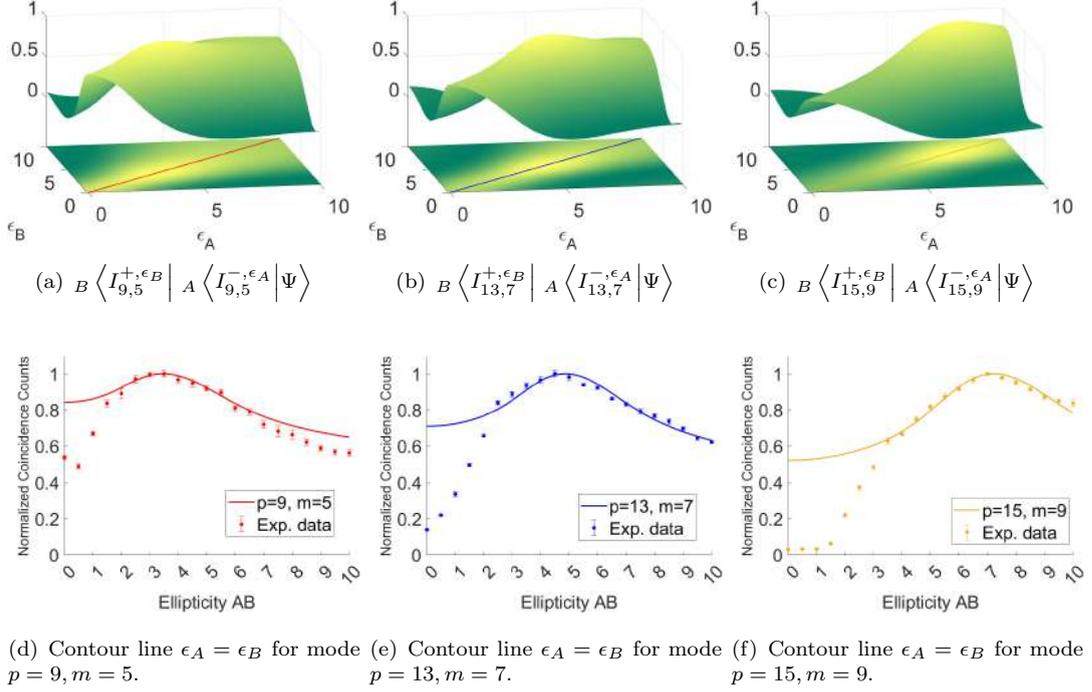
(a) $_B \left\langle I_{9,5}^{+,\epsilon_B} \right| {}_A \left\langle I_{9,5}^{-,\epsilon_A} \middle| \Psi \right\rangle$

(b) $_B \left\langle I_{13,7}^{+,\epsilon_B} \right| {}_A \left\langle I_{13,7}^{-,\epsilon_A} \middle| \Psi \right\rangle$

(c) $_B \left\langle I_{15,9}^{+,\epsilon_B} \right| {}_A \left\langle I_{15,9}^{-,\epsilon_A} \middle| \Psi \right\rangle$

(d) Contour line $\epsilon_A = \epsilon_B$ for mode $p = 9, m = 5$.

(e) Contour line $\epsilon_A = \epsilon_B$ for mode $p = 13, m = 7$.

(f) Contour line $\epsilon_A = \epsilon_B$ for mode $p = 15, m = 9$.

FIGURE 4.1: Comparison of normalized probabilities $_B \left\langle I_{p,m}^{+,\epsilon_B} \right| {}_A \left\langle I_{p,m}^{-,\epsilon_A} \middle| \Psi \right\rangle$ and the experimental data for different modes.

TABLE 4.1: Maximum ellipticity values for the different helicity case

HIG Quantum Numbers	$p = 9, m = 5$	$p = 13, m = 7$	$p = 15, m = 9$
Theoretical ϵ_{AB}	3.5	4.9	7.2
Experimental ϵ_{AB}	3.5	4.5	7.0

However, the measurements for low ϵ values does not match with the theoretical curves. A possible explanation for this is given by the theoretical description of OAM of Ince-Gauss modes given in section 1.2.2. With the objective to explain this let's take the example of measuring the state with the mode $p = 13, m = 7$. As explained in section 3.1.1, to measure a photon in a specific Helical Ince-Gauss mode, we transfer the opposite amount of Orbital Angular Momentum with the Spatial Light Modulator, in order to couple it into a Single Mode Fiber. So, for this mode and low ellipticity values, we need to transfer approximate OAM of 7, but there are other HIG modes that also carry such OAM for this ϵ values, this is shown in Fig. 4.2 b), from which the amount of OAM is almost

the same, for different modes. Qualitatively we can say that the interval where the HIG modes share nearly the same amount of OAM is from $\epsilon \to 0$ to $\epsilon \approx 2$, which is exactly the same interval from where the experimental data does not match with the theoretical description. This can be understood as when we are trying to project the SPDC state in a specific HIG mode with shared OAM with other modes, we are in fact projecting in a mixture of these modes, leading us to lower coincidence counts that the predicted by the theoretical description. This happens also experimentally in the $p = 9, m = 5$ case, where the interval of nearly the same OAM is from $\epsilon \to 0$ to $\epsilon \approx 1$, and also experimentally in the $p = 15, m = 9$ case, where the interval is from $\epsilon \to 0$ to $\epsilon \approx 3$.
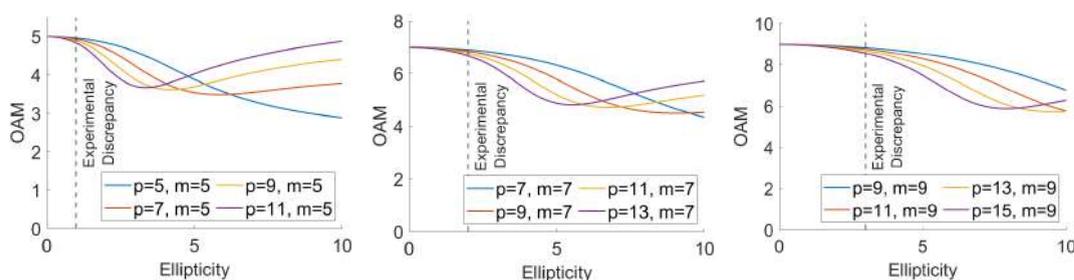
(a) Distinct modes with $m = 5$. Discrepancy line at $\epsilon = 1$.

(b) Distinct modes with $m = 7$. Discrepancy line at $\epsilon = 2$.

(c) Distinct modes with $m = 9$. Discrepancy line at $\epsilon = 3$.

FIGURE 4.2: Expectation value of OAM divided by $\hbar$, for helical Ince-Gauss mode in a single-photon number state. The experimental discrepancy line is placed at the beginning of the ellipticity range in which the experimental and theoretical data agree.

4.2 Probability detection of IG modes with equal helicity

To prove Eq. 2.16, we chose modes as in the earlier section. In order to test the theoretical and experimental capacity we focused on modes that have a maximum global value for the probability detection in our ellipticity interval. We show the modes $p = 11, m = 5$, $p = 12, m = 4$ and $p = 15, m = 7$ for the detection probability given by the squared modulus of Eq. 2.16 in Fig. 4.3 a), b) and c). Each contour line is fixed in the ϵ_A value that maximizes the probability detection for the given mode.

The values of these results seem more dispersed than in the earlier section, because, as we discuss in section 2.2, the probability of finding photons of the SPDC state in HIG modes with the same helicity is small, in contrast with the opposite case, which leads to smaller count rates in the experiment. Since the measurement of photons follows a Poisson distribution [76], then the smaller the count rate, the greater the error in the measurements. This may be the reason why the experimental data does not match the theoretical curve
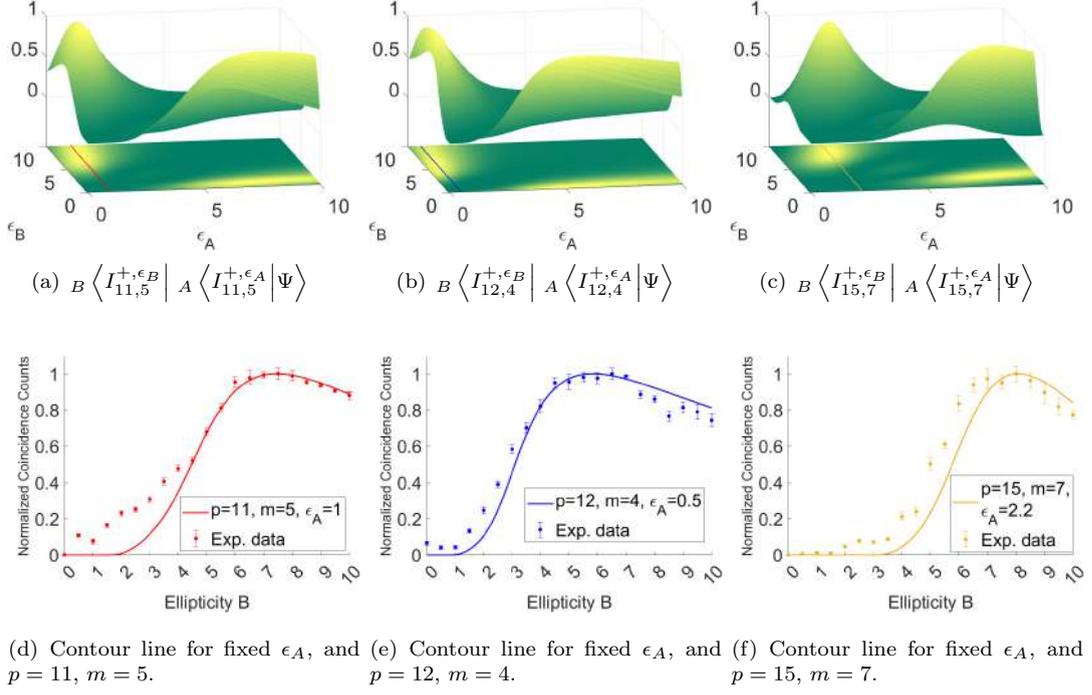
(a) $_B \left\langle I_{11,5}^{+,\epsilon_B} \right| {}_A \left\langle I_{11,5}^{+,\epsilon_A} \middle| \Psi \right\rangle$

(b) $_B \left\langle I_{12,4}^{+,\epsilon_B} \right| {}_A \left\langle I_{12,4}^{+,\epsilon_A} \middle| \Psi \right\rangle$

(c) $_B \left\langle I_{15,7}^{+,\epsilon_B} \right| {}_A \left\langle I_{15,7}^{+,\epsilon_A} \middle| \Psi \right\rangle$

(d) Contour line for fixed ϵ_A, and $p = 11$, $m = 5$.

(e) Contour line for fixed ϵ_A, and $p = 12$, $m = 4$.

(f) Contour line for fixed ϵ_A, and $p = 15$, $m = 7$.

FIGURE 4.3: Comparison of normalized probabilities $_B \left\langle I_{p,m}^{+,\epsilon_B} \right| {}_A \left\langle I_{p,m}^{+,\epsilon_A} \middle| \Psi \right\rangle$ and the experimental data for different modes.

TABLE 4.2: Maximum ellipticity values for the same helicity case

HIG Quantum Numbers	$p = 11, m = 5$	$p = 12, m = 4$	$p = 15, m = 7$
Theoretical ϵ_B	7.5	5.8	8.1
Experimental ϵ_B	7.5	6.5	8.0

in some regions. Even up with that, Figures 4.3 d), e), and f) demonstrate that the experimental and the theory have the same dependence as a function of ellipticity. The experimental data finds its maximum value almost in the same values of the theoretical description. Table 4.2, shows the ϵ_B value at which the maximum probability is reached for these modes.

4.3 Bell-test

In order to prove the form of the state given by Eq. 2.14 we need to confirm the entanglement of the state with the proposed Bell test explained in sections 3.1.1 and 3.1.2. We perform these tests with the modes presented in the earlier sections.

In Fig. 4.4 it is shown the S function given by Eq. 1.51, computed with the joint probability given by Eq. 2.24, at the angles $\theta_A = 0°$, $\theta_B = 22.5°$, $\theta'_A = 45°$, $\theta'_B = 67.5°$, in order to maximize the Bell parameter of the $|\Psi^+\rangle$ state. For the quantum numbers $p = 9$, $m = 5$, the ellipticities $\epsilon_{AB} = 3.5$ were used. For $p = 13$, $m = 7$, we used $\epsilon_{AB} = 5$. And lastly, for $p = 15$, $m = 9$, we used the ellipticities $\epsilon_{AB} = 7$. These ellipticity values are shown as purple dots in Fig 4.4. Table 4.3 shows the measured values of S for this cases.
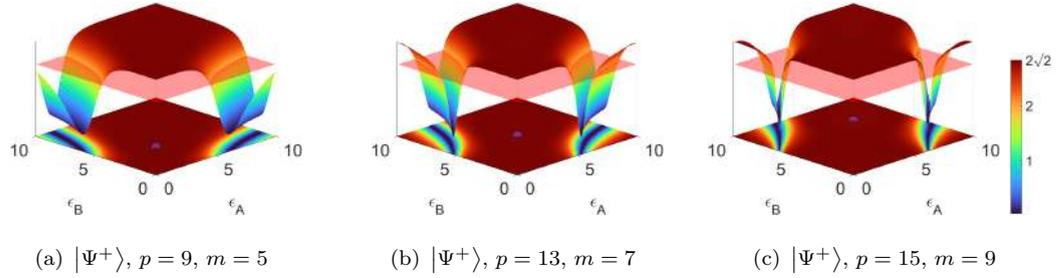

(a) $|\Psi^+\rangle$, $p = 9$, $m = 5$ (b) $|\Psi^+\rangle$, $p = 13$, $m = 7$ (c) $|\Psi^+\rangle$, $p = 15$, $m = 9$

FIGURE 4.4: S value as a function of ϵ_A and ϵ_A for distinct modes, on angles that maximize the violation of the $|\Psi^+\rangle$. The red transparent plane is placed in $S = 2$. The purple dot represents the ϵ_A and ϵ_B values in which the test was experimentally made.

TABLE 4.3: Different entangled HIG Bell states $|\Psi^+\rangle$ and the associated measured value of S.

HIG State	S Exp.	Violation by σ
$p = 9$, $m = 5$, $\epsilon_{A,B} = 3.5$	2.56 ± 0.06	9
$p = 13$, $m = 7$, $\epsilon_{A,B} = 5$	2.30 ± 0.07	4
$p = 15$, $m = 9$, $\epsilon_{A,B} = 7$	2.33 ± 0.09	4

As it is seen, most of the ellipticity values around the diagonal $\epsilon_A = \epsilon_B$, violates the Bell inequality. The experimental values of S, shows values greater than 2, which confirms the entanglement of the state. However none of these values is close to its theorized value $2\sqrt{2}$. This is quite common for Bell measurements in entangled spatial modes [14, 26, 61,

62], and could be due to several reasons; first this can be attributed to the presence of noise, imperfections, or technical constraints in the experimental setup, which can limit the degree of violation that can be achieved. These factors can introduce additional correlations or decrease the observed violation. A way to get rid of this noise detection should be by performing precise quantum state tomography [68, 69].

In Fig. 4.5 it is shown the S function given by Eq. 1.51, computed with the joint probability given by Eq. 2.24, at the angles $\theta_A = 90°$, $\theta_B = 22.5°$, $\theta'_A = 45°$, $\theta'_B = 67.5°$, in order to maximize the Bell parameter of the $|\Phi^+\rangle$ state. For the quantum numbers $p = 11$, $m = 5$, the ellipticities $\epsilon_A = 1$ and $\epsilon_B = 7.5$ were used. For $p = 12$, $m = 4$, we used $\epsilon_A = 0.5$ and $\epsilon_B = 5.5$. And lastly, for $p = 15$, $m = 7$, we used the ellipticities $\epsilon_A = 2.2$ and $\epsilon_B = 8$. These ellipticity values are shown as purple dots in Fig 4.5. Table 4.4 shows the measured values of S for this cases.
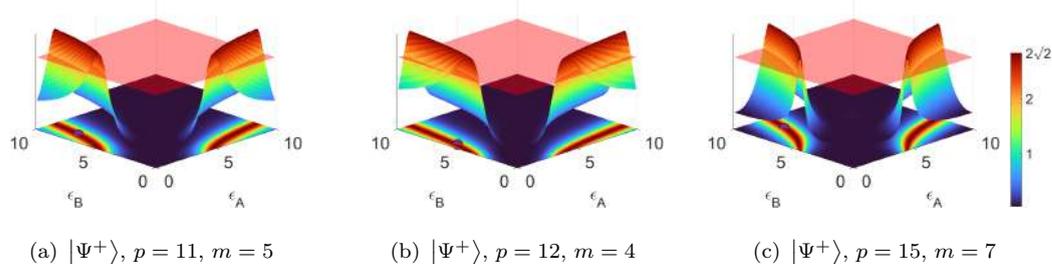

(a) $|\Psi^+\rangle$, $p = 11$, $m = 5$ (b) $|\Psi^+\rangle$, $p = 12$, $m = 4$ (c) $|\Psi^+\rangle$, $p = 15$, $m = 7$

FIGURE 4.5: S value as a function of ϵ_A and ϵ_A for distinct modes, on angles that maximize the violation of the $|\Phi^+\rangle$. The red transparent plane is placed in $S = 2$. The purple dot represents the ϵ_A and ϵ_B values in which the test was experimentally made.

TABLE 4.4: Different entangled HIG Bell states $|\Phi^+\rangle$ and the associated measured value of S.

HIG State	S Exp.	Violation by σ
$p = 11$, $m = 5$, $\epsilon_A = 1$, $\epsilon_B = 7.5$	2.43 ± 0.07	6
$p = 12$, $m = 4$, $\epsilon_A = 0.5$, $\epsilon_B = 5.5$	2.29 ± 0.09	3
$p = 15$, $m = 7$, $\epsilon_A = 2.2$, $\epsilon_B = 8$	2.21 ± 0.08	3

Compared to the previous case, the regions for values of ellipticity, which violates the Bell inequality, are very limited. Even up with that, we were able to violate the Bell inequality experimentally, as the experimental values of S, shows values greater than 2,

which confirms the entanglement of the state. Once again, none of these values is close to its theorized value $2\sqrt{2}$, but the solution to that might be the same as the earlier case.

These results confirm the entanglement and so the Spontaneous Parametric Down-Conversion entangled state represented in Helical Ince-Gauss modes given by Eq. 2.14.

Chapter 5

Conclusions and Future Work

In this thesis, we have explored two photon state, in the terms of Helical Ince-Gaussian basis. Our primary objective was to investigate the description and characterization of the entangled state, given by the Spontaneous Parametric Down-Conversion process, in the Helical Ince-Gauss basis.

By making a change of basis of the photon-pair entangled state, given by SPDC, to Helical the Ince-Gauss basis, we were able to demonstrate, both theoretically and experimentally, how it is possible to tune the probability of finding both down converted photons in Helical Ince-Gauss spatial modes, by tuning the ellipticity parameter of the modes. Even more, we have demonstrated that the entangled state, described in Helical Ince-Gauss modes, is a pair of tunable HIG Bell states, since we are able to change from one symmetric HIG Bell state to another, by only tuning the ellipticity of the modes.

Carrying out Bell tests, in which Bell inequalities were violated, we have experimentally confirmed the entanglement of the state.

This description is useful, as the nowadays quantum protocols require higher-order modes; specifically it can be applied to quantum key distribution protocols, by fixing the ellipticity of the HIG basis in which there is a maximum probability of the state, thus having a useful high-dimensional system, which does not happen in other bases.

In this thesis we have confirmed the entanglement given by these modes, but in order to go any further with this, it is needed to quantify it. By performing precise quantum tomography, for a higher dimension state, as is the current case, it is possible reconstruct the density matrix and quantify the entanglement of the state by calculating quantities like concurrence, the linear entropy, fidelity, to name a few.

Appendix A

MATLAB Codes

In this appendix, the used MATLAB codes to build IG modes are shown. All the subsections are divided into functions. Most of the names of the variables used for these codes correspond to the true name of the quantum numbers of the spatial modes (p, m, l, n), except for ellipticity ϵ that is called as q and σ that is *parity*.

A.1 Code to calculate $A^{\sigma}_{(l+\delta_{\sigma 0})/2}(\epsilon)$

To build IG modes we use 1.16. So first we calculate the Fourier coefficients of the Ince polynomial, by finding the eigenvalues and coefficients, by using tridiagonal matrices from the recurrence relations as the approach of Bandres *et al.* [28, 77]. For the even case $(\sigma = e)$:

```matlab
function [A,n]=AInce(p,m,q,normalization)


%% Check Input
if nargin==4; normalization=0; end;      %
if (m<0)||(m>p); error('ERROR: Wrong range for "m", 0<=m<=p'); end;
if (-1)^(m-p)~=1;    error('ERROR: (p,m) must have the same parity, i.e., (-1)^(m-p)
    =1');   end;


%% Calculate the Coefficients
if mod(p,2)==0
    % p even
    j=p/2;  N=j+1;  n=m/2+1;

    % Matrix
```

```
16       M=diag(q*(j+(1:N-1)),1) + diag([2*q*j,q*(j-(1:N-2))],-1) + diag([0,4*((0:N-2)
         +1).^2]);
17       if p==0; M=0; end;
18
19       % Eigenvalues and Eigenvectors
20       [A,ets]=eig(M);
21       ets=diag(ets);
22       [ets,index]=sort(ets);
23       A=A(:,index);
24
25       % Normalization
26       if normalization==0;
27           N2=2*A(1,n).^2+sum(A(2:N,n).^2);
28           NS=sign(sum(A(:,n)));
29           A=A/sqrt(N2)*NS;
30       else
31           mv=(2:2:p).';
32           N2=sqrt(A(1,n)^2*2*gamma(p/2+1)^2+sum((sqrt(gamma((p+mv)/2+1).*gamma((p-mv)
         /2+1) ).*A(2:p/2+1,n)).^2 ));
33           NS=sign(sum(A(:,n)));
34           A=A/N2*NS;
35       end
36
37
38  else
39       % p odd
40       j=(p-1)/2;   N=j+1;   n=(m+1)/2;
41
42       % Matrix
43       M=diag(q/2*(p+(2*(0:N-2)+3)),1)+diag(q/2*(p-(2*(1:N-1)-1)),-1) + diag([q/2+p*q
         /2+1,(2*(1:N-1)+1).^2]);
44
45       % Eigenvalues and Eigenvectors
46       [A,ets]=eig(M);
47       ets=diag(ets);
48       [ets,index]=sort(ets);
49       A=A(:,index);
50
51       % Normalization
52       if normalization==0;
53           N2=sum(A(:,n).^2);
54           NS=sign(sum(A(:,n)));
55           A=A/sqrt(N2)*NS;
56       else
57           mv=(1:2:p).';
58           N2=sqrt(sum( ( sqrt(gamma((p+mv)/2+1).*gamma((p-mv)/2+1) ).*A(:,n)).^2 ));
59           NS=sign(sum(A(:,n)));
60           A=A/N2*NS;
61       end
62
63  end
64
```

```
65 | return
```

For the odd case ($\sigma = o$):

```matlab
1  | function [A,n]=BInce(p,m,q,normalization)
2  |
3  |
4  | %% Check Input
5  | if nargin==4; normalization=0; end;       %
6  | if (m<1)||(m>p);   error('ERROR: Wrong range for "m", 1<=m<=p'); end;
7  | if (-1)^(m-p)~=1;    error('ERROR: (p,m) must have the same parity, i.e., (-1)^(m-p)
   |     =1'); end;
8  |
9  | %% Calculate the Coefficients
10 | if mod(p,2)==0
11 |     % p even
12 |     j=p/2;   N=j+1; n=m/2;
13 |
14 |     % Matrix
15 |     M=diag(q*(j+(2:N-1)),1)+diag(q*(j-(1:N-2)),-1) + diag(4*((0:N-2)+1).^2);
16 |
17 |     % Eigenvalues and Eigenvectors
18 |     [A,ets]=eig(M);
19 |     ets=diag(ets);
20 |     [ets,index]=sort(ets);
21 |     A=A(:,index);
22 |
23 |     % Normalization
24 |     r=1:N-1;
25 |     if normalization==0;
26 |         N2=sum(A(:,n).^2);
27 |         NS=sign(sum(r.*transpose(A(:,n))));
28 |         A=A/sqrt(N2)*NS;
29 |     else
30 |         mv=(2:2:p).';
31 |         N2=sqrt(sum((sqrt(gamma((p+mv)/2+1).*gamma((p-mv)/2+1) ).*A(:,n)).^2 ));
32 |         NS=sign(sum(r.*A(:,n)'));
33 |         A=A/N2*NS;
34 |     end
35 |
36 | else
37 |     % p odd
38 |     j=(p-1)/2; N=j+1; n=(m+1)/2;
39 |
40 |     % Matrix
41 |     M=diag(q/2*(p+(2*(0:N-2)+3)),1)+diag(q/2*(p-(2*(1:N-1)-1)),-1) + diag([-q/2-p*q
   |     /2+1,(2*(1:N-1)+1).^2]);
42 |
43 |     % Eigenvalues and Eigenvectors
44 |     [A,ets]=eig(M);
45 |     ets=diag(ets);
46 |     [ets,index]=sort(ets);
```

```
47        A=A( : , index ) ;
48
49        % Normalization
50        r =2*(0:N−1)+1;
51        if  normalization==0;
52            N2=sum(A( : , n ) . ˆ 2 ) ;
53            NS=sign (sum( r .* transpose (A( : , n ) ) ) ) ;
54            A=A/ sqrt (N2)*NS;
55        else
56            mv = (1:2:p ) . ' ;
57            N2=sqrt (sum(  (  sqrt (gamma((p+mv)/2+1) .* gamma((p−mv)/2+1)  ) .*A( : , n ) ) . ˆ 2  ) ) ;
58            NS=sign (sum( r .*A( : , n ) ' ) ) ;
59            A=A/N2*NS;
60        end
61
62 end
63
64 return
```

A.2   Code to calculate $D_{ln}^{\sigma}(\epsilon)$

First we calculate the coefficients without normalization:

```
1  function  [D0]=DInce (p,m,q, n, l , parity )
2  %%%
3  %parity=0  even ,  =1  odd
4  normalization =0;
5
6
7  if  parity==0 %even
8      [A, ra]=AInce (p,m,q, normalization ) ;
9      D0=((−1)ˆ(n+l+(p+m) /2) )*( sqrt (2* factorial (n+l )* factorial (n) ) )*A( floor ( ( l )/2)+1,
       ra ) ;
10 else %odd
11     if  l==0
12         D0=0;
13     else
14         [B, rb]=BInce (p,m,q, normalization ) ;
15         D0=((−1)ˆ(n+l+(p+m) /2) )*( sqrt (2* factorial (n+l )* factorial (n) ) )*B( floor ( ( l +1)
       /2) , rb ) ;
16     end
17 end
18
19 return
20 %%%
```

Then we found the normalization constant $\mathfrak{D}$, and then calculate the $D_{ln}^{\sigma}(\epsilon)$ coefficients:

```matlab
1   function D= Dnorm(p,m,q,ni,li,parity)
2
3   v_par = [];
4   v_impar = [];
5   indicesl=[];
6   indicesn=[];
7
8   %parity=0 even, =1 odd
9
10  for l =0:p
11      for n=0:p
12          if p==2*n+l
13              v_par = [v_par, DInce(p,m,q,n,l,0)];
14              v_impar = [v_impar, DInce(p,m,q,n,l,1)];
15              indicesl=[indicesl, l];
16              indicesn=[indicesn, n];
17          end
18      end
19  end
20
21  Dn1p=sum(v_par.^2,'all');
22  Dnp=1/sqrt(Dn1p);
23  De_0=v_par.*Dnp;
24
25  Dn1i=sum(v_impar.^2,'all');
26  Dni=1/sqrt(Dn1i);
27  Do_0=v_impar.*Dni;
28
29  Do = [Do_0(:), indicesn(:), indicesl(:)];
30  De = [De_0(:), indicesn(:), indicesl(:)];
31
32  S=0;
33
34  [max,equis]=size(Do);
35
36  for i =1:max
37      if Do(i,2)==ni
38          if Do(i,3)==li
39              if parity==1
40                  D=Do(i,1);
41              else
42                  D=De(i,1);
43              end
44          end
45      end
46  end
47
48  return
```

A.3   Code to construct Helical Ince-Gauss modes

We construct the HIG modes with the even and odd IG modes, which are a superposition of even and odd LG modes. So first we construct even and odd LG 1.11:

```
1  function LGe=LGeven(l,n,w,x,y)
2
3  r=sqrt(x.^2+y.^2);
4  theta=atan2(y,x);
5  LGP=laguerre(n,abs(l),(2*r.^2/w^2));
6  LGe=(((4*factorial(n))/(pi*factorial(n+l)))^(1/2))*(1/w)*cos(theta.*l).*(r.*(2)
       ^(1/2)/w).^l.*LGP.*exp(-r.^2/w^2);
7
8  return
```

```
1  function LGo=LGodd(l,n,w,x,y)
2
3  r=sqrt(x.^2+y.^2);
4  theta=atan2(y,x);
5  LGP=laguerre(n,abs(l),(2*r.^2/w^2));
6  LGo=(((4*factorial(n))/(pi*factorial(n+l)))^(1/2))*(1/w)*sin(theta.*l).*(r.*(2)
       ^(1/2)/w).^l.*LGP.*exp(-r.^2/w^2);
7
8  return
```

Where we have used a more efficient Laguerre function than the one offered by the MATLAB for default:

```
1  function y=laguerre(p,l,x)
2
3  y=zeros(p+1,1);
4  if p==0
5      y=1;
6  else
7  for m=0:p
8      y(p+1-m)=((-1).^m.*(factorial(p+l)))./(factorial(p-m).*factorial(l+m).*
       factorial(m));
9  end
10 end
11 y=polyval(y,x);
12 end
```

Now we build the even and odd IG modes 1.15 with the earlier calculated coefficients $D_{ln}^{\sigma}(\epsilon)$:

```
1  function IGe=IGeven(p,m,q,w,x,y)
2
3  IGe= 0;
4
```

```
5  for l =0:p
6      for n=0:p
7          if p==2*n+l
8              LGe=LGeven(l,n,w,x,y);
9              if max(LGe,[],"all")==0
10                 IGe= IGe+Dnorm(p,m,q,n,l,0).*LGe;
11             else
12                 IGe= IGe+Dnorm(p,m,q,n,l,0).*LGe;
13             end
14         end
15     end
16 end
17
18 return
```

```
1  function IGo=IGodd(p,m,q,w,x,y)
2
3  IGo= 0;
4
5  for l =0:p
6      for n=0:p
7          if p==2*n+l
8              LGo=LGodd(l,n,w,x,y);
9              if max(LGo,[],"all")==0
10                 IGo= IGo+Dnorm(p,m,q,n,l,1).*LGo;
11             else
12                 IGo= IGo+Dnorm(p,m,q,n,l,1).*LGo;
13             end
14         end
15     end
16 end
17
18 return
```

Finally, we can construct the Helical Ince-Gauss modes as 1.17:

```
1  function IGH=IGH(p,m,q,w,sign,x,y)
2  %sign=0 positive, so: (IGe+1i.*IGo)/sqrt(2)
3  %sign=1 negative, so: (IGe-1i.*IGo)/sqrt(2)
4  IGe=IGeven(p,m,q,w,x,y);
5  IGo=IGodd(p,m,q,w,x,y);
6
7  if sign==0
8      IGH=(IGe+1i.*IGo)/sqrt(2);
9  else
10     IGH=(IGe-1i.*IGo)/sqrt(2);
11 end
12
13 return
```

Bibliography

[1] M. B. Nielsen and I. L. Chuang, *Quantum Computation and Quantum Information: 10th Anniversary Edition*. 1 2011.

[2] R. Horodecki, P. Horodecki, M. Horodecki, and K. Horodecki, "Quantum entanglement," *Reviews of Modern Physics*, vol. 81, pp. 865–942, 2 2007.

[3] O. Gühne and G. Tóth, "Entanglement detection," *Physics Reports*, vol. 474, pp. 1–75, 4 2009.

[4] A. Einstein, B. Podolsky, and N. Rosen, "Can Quantum-Mechanical Description of Physical Reality Be Considered Complete?," *Physical Review*, vol. 47, pp. 777–780, 5 1935.

[5] J. Bell, "On the Einstein Podolsky Rosen paradox," *Physics*, vol. 1, pp. 195–200, 11 1964.

[6] J. F. Bell, M. A. Horne, and A. Zeilinger, "Speakable and Unspeakable in Quantum Mechanics," *American Journal of Physics*, vol. 57, p. 567, 6 1989.

[7] J. J. W. Clauser, M. A. Horne, A. Shimony, and R. I. G. Holt, "Proposed Experiment to Test Local Hidden-Variable Theories," *Physical Review Letters*, vol. 23, pp. 880–884, 10 1969.

[8] A. Aspect, P. Grangier, and G. Roger, "Experimental Tests of Realistic Local Theories via Bell's Theorem," *Physical Review Letters*, vol. 47, pp. 460–463, 8 1981.

[9] L. K. Shalm, D. R. Hamel, Z. Yan, C. Simon, K. J. Resch, and T. Jennewein, "Three-photon energy–time entanglement," *Nature Physics*, vol. 9, pp. 19–22, 11 2012.

[10] A. Cuevas, G. Carvacho, G. Saavedra, J. Cariñe, W. A. T. Nogueira, M. Figueroa, A. Cabello, P. Mataloni, G. Lima, and G. B. Xavier, "Long-distance distribution of genuine energy-time entanglement," *Nature Communications*, vol. 4, 11 2013.

[11] J. C. Howell, R. S. Bennink, S. J. Bentley, and R. W. Boyd, "Realization of the Einstein-Podolsky-Rosen Paradox Using Momentum- and Position-Entangled Photons from Spontaneous Parametric Down Conversion," *Physical Review Letters*, vol. 92, 5 2004.

[12] K. Zielnicki, K. Garay-Palmett, D. Cruz-Delgado, H. Cruz-Ramirez, M. F. O'Boyle, B. Fang, V. O. Lorenz, A. B. U'Ren, and P. G. Kwiat, "Joint spectral characterization of photon-pair sources," *Journal of Modern Optics*, vol. 65, pp. 1141–1160, 2 2018.

[13] D. L. Andrews and M. Babiker, *The Angular Momentum of Light.* 11 2012.

[14] J. K. Leach, B. Jack, J. L. Romero, M. Ritsch-Marte, R. W. Boyd, A. Jha, S. M. Barnett, S. Franke-Arnold, and M. J. Padgett, "Violation of a Bell inequality in two-dimensional orbital angular momentum state-spaces," *Optics Express*, vol. 17, p. 8287, 5 2009.

[15] C. Couteau, "Spontaneous parametric down-conversion," *Contemporary Physics*, vol. 59, pp. 291–304, 8 2018.

[16] A. Mair, A. Vaziri, G. Weihs, and A. Zeilinger, "Entanglement of the orbital angular momentum states of photons," *Nature*, vol. 412, pp. 313–316, 7 2001.

[17] L. Allen, M. W. Beijersbergen, R. J. C. Spreeuw, and J. P. Woerdman, "Orbital angular momentum of light and the transformation of Laguerre-Gaussian laser modes," *Physical Review A*, vol. 45, pp. 8185–8189, 6 1992.

[18] G. Calvo, A. Picon, and E. Bagan, "Quantum field theory of photons with orbital angular momentum," *Physical Review A*, vol. 73, 1 2006.

[19] S. J. Van Enk and G. Nienhuis, "Spin and Orbital Angular Momentum of Photons," *EPL*, vol. 25, pp. 497–501, 3 1994.

[20] M. Krenn, M. Malik, M. Erhard, and A. Zeilinger, "Orbital angular momentum of photons and the entanglement of Laguerre–Gaussian modes," *Philosophical Transactions of the Royal Society A*, vol. 375, p. 20150442, 2 2017.

[21] X. F. Ren, G. P. Guo, Y. F. Huang, C. F. Li, and G. C. Guo, "Plasmon-assisted transmission of high-dimensional orbital angular-momentum entangled state," *EPL*, vol. 76, pp. 753–759, 12 2006.

[22] N. Tischler, I. Fernandez-Corbaton, X. Zambrana-Puyalto, A. Minovich, X. Vidal, M. L. Juan, and G. K. Brennen, "Experimental control of optical helicity in nanophotonics," *Light-Science Applications*, vol. 3, p. e183, 6 2014.

[23] M. Mafu, A. Dudley, S. Goyal, D. Giovannini, M. McLaren, M. J. Padgett, T. R. Konrad, F. Petruccione, N. Lütkenhaus, and A. Forbes, "Higher-dimensional orbital-angular-momentum-based quantum key distribution with mutually unbiased bases," *Physical Review A*, vol. 88, 9 2013.

[24] M. Mirhosseini, O. S. Magaña-Loaiza, M. N. O'Sullivan, B. Rodenburg, M. Malik, M. P. J. Lavery, M. J. Padgett, D. J. Gauthier, and R. W. Boyd, "High-dimensional quantum cryptography with twisted light," *New Journal of Physics*, vol. 17, p. 033033, 3 2015.

[25] S. P. Walborn, S. Pádua, and C. H. Monken, "Conservation and entanglement of Hermite-Gaussian modes in parametric down-conversion," *Physical Review A*, vol. 71, 5 2005.

[26] M. McLaren, M. Agnew, J. Leach, F. S. Roux, M. J. Padgett, R. W. Boyd, and A. Forbes, "Entangled Bessel-Gaussian beams," *Optics Express*, vol. 20, p. 23589, 10 2012.

[27] J. Tang, Y. Ming, Z.-X. Chen, W. Hu, F. Xu, and Y.-Q. Lu, "Entanglement of photons with complex spatial structure in Hermite-Laguerre-Gaussian modes," *Physical review*, vol. 94, 7 2016.

[28] M. A. Bandres and J. C. Gutiérrez-Vega, "Ince–Gaussian modes of the paraxial wave equation and stable resonators," *Journal of the Optical Society of America*, vol. 21, p. 873, 5 2004.

[29] M. A. Bandres and J. C. Gutiérrez-Vega, "Ince–Gaussian beams," *Optics Letters*, vol. 29, p. 144, 1 2004.

[30] W. N. Plick, M. Krenn, R. Fickler, S. Ramelow, and A. Zeilinger, "Quantum orbital angular momentum of elliptically symmetric light," *Physical Review A*, vol. 87, 3 2013.

[31] M. Krenn, R. Fickler, M. Huber, R. Lapkiewicz, W. N. Plick, S. Ramelow, and A. Zeilinger, "Entangled singularity patterns of photons in Ince-Gauss modes," *Physical Review A*, vol. 87, 1 2013.

[32] B. E. A. Saleh, M. C. Teich, and R. E. Slusher, *Fundamentals of Photonics*. 4 2016.

[33] H. Laabs and B. Ozygus, "Excitation of Hermite Gaussian modes in end-pumped solid-state lasers via off-axis pumping," *Optics and Laser Technology*, vol. 28, pp. 213–214, 4 1996.

[34] M. W. Cox, L. Maqondo, R. Kara, G. Milione, L. Cheng, and A. Forbes, "The Resilience of Hermite– and Laguerre–Gaussian Modes in Turbulence," *Journal of Lightwave Technology*, vol. 37, pp. 3911–3917, 8 2019.

[35] H. Sun, K. Liu, Z.-L. Liu, G. Pengliang, J. Zhang, and J. Gao, "Small-displacement measurements using high-order Hermite-Gauss modes," *Applied Physics Letters*, vol. 104, 3 2014.

[36] M. Lassen, V. Delaubert, C. C. Harb, P. K. Lam, N. Treps, and H.-A. Bachor, "Generation of Squeezing in Higher Order Hermite - Gaussian Modes with an Optical Parametric Amplifier," *Journal of the European Optical Society: Rapid Publications*, vol. 1, 6 2006.

[37] T. Doster and A. T. Watnik, "Laguerre–Gauss and Bessel–Gauss beams propagation through turbulence: analysis of channel efficiency," *Applied optics*, vol. 55, p. 10239, 12 2016.

[38] A. Minoofar, X. Su, H. Zhou, R. Zhang, F. Alishahi, K. Zou, H. Song, K. Pang, S. Zach, M. Tur, A. F. Molisch, H. Sasaki, D. Lee, and A. E. Willner, "Experimental Demonstration of Sub-THz Wireless Communications Using Multiplexing of Laguerre-Gaussian Beams When Varying two Different Modal Indices," *Journal of Lightwave Technology*, vol. 40, pp. 3285–3292, 5 2022.

[39] W. Wang, T. Yokozeki, R. Ishijima, M. Takeda, and S. G. Hanson, "Optical vortex metrology based on the core structures of phase singularities in Laguerre-Gauss transform of a speckle pattern," *Optics Express*, vol. 14, p. 10195, 1 2006.

[40] N. H. Valencia, V. Srivastav, S. Leedumrongwatthanakun, W. McCutcheon, and M. Malik, "Entangled ripples and twists of light: radial and azimuthal Laguerre–Gaussian mode entanglement," *Journal of Optics*, vol. 23, p. 104001, 9 2021.

[41] F. Zhu, S. Huang, W. Shao, J. Zhang, M. Chen, W. Zhang, and J.-Z. Zeng, "Free-space optical communication link using perfect vortex beams carrying orbital angular momentum (OAM)," *Optics Communications*, vol. 396, pp. 50–57, 8 2017.

[42] Z. Sun, J. Wang, Z. Li, T. Wu, Y. Yang, Y. Liu, and Y. Lu, "Stable propagation of Ince-Gaussian vector beams through atmospheric turbulence," *Optics Communications*, vol. 515, p. 128193, 7 2022.

[43] C. Alpmann, M. Woerdemann, and C. Denz, "Tailored Light Fields: A Novel Approach for Creating Complex Optical Traps," *Optics Photonics News*, vol. 22, p. 28, 12 2011.

[44] S. K. Singh, H. Haginaka, B. J. Jackin, K. Kinashi, N. Tsutsumi, and W. Sakai, "Generation of Ince–Gaussian Beams Using Azocarbazole Polymer CGH," *Journal of Imaging*, vol. 8, p. 144, 5 2022.

[45] B. Baghdasaryan and S. Fritzsche, "Enhanced entanglement from Ince-Gaussian pump beams in spontaneous parametric down-conversion," *Physical review*, vol. 102, 11 2020.

[46] H. Yang, H. Wu, W. Gao, C. Rosales-Guzmán, and Z.-H. Zhu, "Parametric upconversion of Ince–Gaussian modes," *Optics Letters*, vol. 45, p. 3034, 5 2020.

[47] J. H. Poynting, "XV. On the transfer of energy in the electromagnetic field," ., vol. 175, pp. 343–361, 1 1884.

[48] K. Dholakia and T. Čižmár, "Shaping the future of manipulation," *Nature Photonics*, vol. 5, no. 6, pp. 335–342, 2011.

[49] N. M. Litchinitser, "Structured Light Meets Structured Matter," *Science*, vol. 337, no. 6098, pp. 1054–1055, 2012.

[50] S. W. Hell and J. Wichmann, "Breaking the diffraction resolution limit by stimulated emission: stimulated-emission-depletion fluorescence microscopy," *Optics Letters*, vol. 19, no. 11, p. 780, 1994.

[51] G. Xie, H. Song, Z. Zhao, G. Milione, Y. Ren, C. Liu, R. Zhang, C. Bao, L. Li, Z. Wang, K. Pang, D. Starodubov, B. Lynn, M. Tur, and A. E. Willner, "Using a complex optical orbital-angular-momentum spectrum to measure object parameters," *Optics Letters*, vol. 42, no. 21, p. 4482, 2017.

[52] S. S. Yuan, J. Wu, M. L. Chen, Z. Lan, L. Zhang, S. Sun, Z. Huang, X. Chen, S. Zheng, L. J. Jiang, X. Zhang, and W. E. Sha, "Approaching the Fundamental Limit of Orbital-Angular-Momentum Multiplexing Through a Hologram Metasurface," *Physical Review Applied*, vol. 16, no. 6, 2021.

[53] S. M. Barnett and L. J. Allen, "Orbital angular momentum and nonparaxial light beams," *Optics Communications*, vol. 110, pp. 670–678, 9 1994.

[54] A. Zeilinger, G. Weihs, T. Jennewein, and M. Aspelmeyer, "Happy centenary, photon," *Nature*, vol. 433, pp. 230–238, 1 2005.

[55] S. M. Barnett, A. Beige, A. Ekert, B. M. Garraway, C. H. Keitel, V. Kendon, M. Lein, G. J. Milburn, H. M. Moya-Cessa, M. Murao, J. K. Pachos, G. M. Palma, E. Paspalakis, S. J. D. Phoenix, B. Piraux, M. B. Plenio, B. C. Sanders, J. Twamley,

A. Vidiella-Barranco, and M. J. Kim, "Journeys from quantum optics to quantum technology," *Progress in Quantum Electronics*, vol. 54, pp. 19–45, 8 2017.

[56] S. J. Van Enk and G. Nienhuis, "Commutation Rules and Eigenvalues of Spin and Orbital Angular Momentum of Radiation Fields," *Journal of Modern Optics*, vol. 41, pp. 963–977, 5 1994.

[57] T. Jennewein, M. Barbieri, and A. J. P. White, "Single-photon device requirements for operating linear optics quantum computing outside the post-selection basis," *Journal of Modern Optics*, vol. 58, pp. 276–287, 2 2011.

[58] A. Joobeur, B. E. A. Saleh, and M. C. Teich, "Spatiotemporal coherence properties of entangled light beams generated by parametric down-conversion," *Physical Review A*, vol. 50, pp. 3349–3361, 10 1994.

[59] J. P. Torres, C. I. Osorio, and L. Torner, "Orbital angular momentum of entangled counterpropagating photons," *Optics Letters*, vol. 29, p. 1939, 8 2004.

[60] F. M. Miatto, A. M. Yao, and S. M. Barnett, "Full characterization of the quantum spiral bandwidth of entangled biphotons," *Physical Review A*, vol. 83, 3 2011.

[61] A. C. Dada, J. Leach, G. S. Buller, M. J. Padgett, and E. Andersson, "Experimental high-dimensional two-photon entanglement and violations of generalized Bell inequalities," *Nature Physics*, vol. 7, pp. 677–680, 5 2011.

[62] D. Zhang, X. Qiu, W. Zhang, and L. Chen, "Violation of a Bell inequality in two-dimensional state spaces for radial quantum number," *Physical review*, vol. 98, 10 2018.

[63] N. Friis, G. Vitagliano, M. Malik, and M. Huber, "Entanglement certification from theory to experiment," *Nature Reviews Physics*, vol. 1, pp. 72–87, 12 2018.

[64] J. Von Neumann, *Mathematical Foundations of Quantum Mechanics*. 4 2018.

[65] S. Hill and W. K. Wootters, "Entanglement of a Pair of Quantum Bits," *Physical Review Letters*, vol. 78, pp. 5022–5025, 6 1997.

[66] R. Penrose, "Quantum computation, entanglement and state reduction," *Philosophical Transactions of the Royal Society A*, vol. 356, pp. 1927–1939, 8 1998.

[67] M. Gupta and M. J. Nene, "Quantum Computing: An Entanglement Measurement," 12 2020.

[68] R. Thew, K. Nemoto, A. White, and W. J. Munro, "Qudit quantum-state tomography," *Physical Review A*, vol. 66, 1 2002.

[69] B. Jack, J. K. Leach, H. Ritsch, S. M. Barnett, M. J. Padgett, and S. Franke-Arnold, "Precise quantum tomography of photon pairs with entangled orbital angular momentum," *New Journal of Physics*, vol. 11, p. 103024, 10 2009.

[70] M. J. Padgett and J. Courtial, "Poincaré-sphere equivalent for light beams containing orbital angular momentum," *Optics Letters*, vol. 24, p. 430, 4 1999.

[71] C. Maurer, A. Jesacher, S. Bernet, and M. Ritsch-Marte, "What spatial light modulators can do for optical microscopy," *Laser Photonics Reviews*, vol. 5, pp. 81–101, 12 2010.

[72] S. Reichelt, R. Häussler, G. Fütterer, N. Leister, H. Kato, N. Usukura, and Y. Kanbayashi, "Full-range, complex spatial light modulator for real-time holography," *Optics Letters*, vol. 37, p. 1955, 5 2012.

[73] H.-H. Lu, Y.-P. Lin, P.-Y. Wu, C.-Y. Chen, M.-C. Chen, and T.-W. Jhang, "A multiple-input-multiple-output visible light communication system based on VCSELs and spatial light modulators," *Optics Express*, vol. 22, p. 3468, 2 2014.

[74] R. W. Cohn, "Fundamental properties of spatial light modulators for the approximate optical computation of Fourier transforms: a review," *Optical Engineering*, vol. 40, p. 2452, 11 2001.

[75] J. B. Bentley, J. A. Davis, M. A. Bandres, and J. C. Gutiérrez-Vega, "Generation of helical Ince-Gaussian beams with a liquid-crystal display," *Optics Letters*, vol. 31, p. 649, 3 2006.

[76] C. Gerry, P. Knight, and P. L. Knight, *Introductory Quantum Optics.* Cambridge University Press, 1 2005.

[77] M. A. Bandres, MATLAB Central File Exchange., "Ince polynomials." `https://la.mathworks.com/matlabcentral/fileexchange/44932-ince-polynomials`, 2023.

[78] Y. Lian, X. Qi, Y. Wang, Z. Bai, Y. Wang, and Z. Lu, "OAM beam generation in space and its applications: A review," *Optics and Lasers in Engineering*, vol. 151, p. 106923, 4 2022.